1-14-2019

Electron density topological and adsorbate orbital analyses of water and carbon monoxide co-adsorption on platinum

Nicholas Dimakis

Isaiah Salas

Luis Gonzalez

Neili Loupe

Eugene S. Smotkin

Electron Density Topological and Adsorbate Orbital Analyses of Water and Carbon Monoxide Co-adsorption on Platinum

*Nicholas Dimakis, [1]*Isaiah Salas, [2] Luis Gonzalez, [3] Neili Loupe, [4] and Eugene S. Smotkin[4]*

[1] Department of Physics and Astronomy, University of Texas Rio Grande Valley, Edinburg, TX, USA

[2]Achieve Early College High School, McAllen, TX, USA

[3]PSJA Thomas Jefferson T-STEM Early College HS, Pharr, TX, USA

[4]Department of Chemistry and Chemical Biology, Northeastern University, Boston, MA, USA

AUTHOR INFORMATION

Corresponding Author

*1201 W. University Drive, Edinburg, TX 78539; Phone: (956) 665-8761; Email: nicholas.dimakis@utrgv.edu

ABSTRACT

The electron density topology of carbon monoxide (CO) on dry and hydrated platinum is evaluated under the quantum theory of atoms in molecules (QTAIM) and by adsorbate orbital approaches. The impact of water co-adsorbate on the electronic, structural, and vibrational properties of CO on Pt are modelled by periodic density functional theory (DFT). At low CO coverage, increased hydration weakens C-O bonds and strengthens C-Pt bonds, as verified by changes in bond lengths and stretching frequencies. These results are consistent with QTAIM, the 5σ donation-$2\pi^*$ backdonation model, and our extended π-attraction σ-repulsion model (extended π-σ model). This work links changes in the non-zero eigenvalues of the electron density Hessian at QTAIM bond critical points to changes in the π and σ C-O bonds with systematic variation of CO/H_2O co-adsorbate scenarios. QTAIM invariably shows bond strengths and lengths as being negatively correlated. For atop CO on hydrated Pt, QTAIM and phenomenological models are consistent with a direct correlation between C-O bond strength and CO coverage. However, DFT modelling in the absence of hydration show that C-O bond lengths are not negatively correlated to their stretching frequencies, in contrast to the Badger rule: When QTAIM and phenomenological models do not agree, the use of the non-zero eigenvalues of the electron density Hessian as inputs to the phenomenological models, aligns them with QTAIM. The C-O and C-Pt bond strengths of bridge and three-fold bound CO on dry and hydrated platinum are also evaluated by QTAIM and adsorbate orbital analyses.

1. INTRODUCTION

1.1. Background

Carbon monoxide has a greater affinity for fuel cell Pt catalysts than does hydrogen[1]. This is compounded by the fact that hydrogen fuel cell anode potentials of are never sufficiently positive to oxidize adsorbed CO (CO_{ads}) to CO_2.[2] Hence, transition metals, alloyed or mixed phase with Pt, are used to lower the CO adsorption energy (E_{ads}). This is known as the ligand effect.[3] In direct methanol fuel cells, where the anode can be as high as 300 mV vs RHE, transition metals (e.g., Ru) lower the activation energy by activating water for oxygen transfer to CO_{ads} (Ref. 2). The key components for theoretical analyses of hydrogen and direct oxidation fuel cells are CO, water, and the catalyst structure.[4, 5]

CO adsorption on transition metals and alloys are described by phenomenological and catalyst d-band models (Nørskov d-band center[6] and our d-band dispersion[7] model). The phenomenological models include: 1) Blyholder-type models[8] 2) the Nilsson and co-workers[9-13] π-attraction and σ-repulsion (π-σ) model and most recently 3) the Dimakis-Smotkin extended π-σ model.[14-17]

Blyholder-type models: Upon adsorption on Pt, the internal CO_{ads} bond weakens (C-O stretching frequency-ν_{CO}- downshifts) and a stable C-Pt bond is formed.[18-20] This is explained by a 5σ donation-2π* backdonation model, also known as the "Blyholder model". The original Blyholder model was limited to π-molecular orbital contributions to the adsorption process (1π and 2π*). The effect of the 5σ donation was added later.[21] Although the 5σ donation-2π* backdonation model successfully explains CO adsorption on a variety of metals including Pt,[22] it fails for CO_{ads} on Pt-based alloys.[23]

Nilsson π-attraction and σ-repulsion (π-σ) model: The Nilsson π-σ model improved upon the 5σ donation-2π* backdonation model by considering the influence of charge polarization effects

3

over the entire set of σ and π CO-substrate orbitals. The hybridization of the CO molecular orbitals with the metal orbitals yield hybrid adsorbate-substrate tilde-type orbitals. The $\tilde{\pi}$-system contains three orbitals/bands: the $1\tilde{\pi}$, the $d_{\tilde{\pi}}$ and the $2\tilde{\pi}^*$-bands. The $1\tilde{\pi}$ orbital is both C-O and C-Metal bonding, whereas the $2\tilde{\pi}^*$-band is C-O antibonding and C-Metal bonding. The $d_{\tilde{\pi}}$-band is a hybrid of the 1π and $2\pi^*$ CO molecular orbitals mixed with the metal $d_{xz,yz}$-band. The $d_{\tilde{\pi}}$-band extends from a lower energy region dominated by oxygen lone pair electrons and heavily weighted by a 1π contribution (i.e., C-O bonding), to a higher energy region extending to the Fermi level with a heavy $2\pi^*$ contribution (i.e., C-O antibonding). While the π-σ model does not explicitly invoke direct backdonation to the CO region of the $2\tilde{\pi}^*$, such backdonation is certainly inferred by the presence of the C-O antibonding $d_{\tilde{\pi}}$ high energy region that weakens the internal CO_{ads} bond. The decreased $1\tilde{\pi}$ polarization towards oxygen also contributes to the internal CO_{ads} bond weakening.

The $\tilde{\sigma}$-system also contains three orbitals/bands: the $4\tilde{\sigma}$ and $5\tilde{\sigma}$ orbitals and the $d_{\tilde{\sigma}}$-band. The $4\tilde{\sigma}$ and $5\tilde{\sigma}$ orbitals are C-Metal bonding, whereas the $d_{\tilde{\sigma}}$-band is C-Metal antibonding. Moreover, the $4\tilde{\sigma}$ and the $d_{\tilde{\sigma}}$-band are C-O antibonding, whereas the $5\tilde{\sigma}$ is weekly bonding. The free CO 4σ and 5σ molecular orbitals are polarized towards oxygen and carbon, respectively. Upon hybridization with metal orbitals, the $4\tilde{\sigma}$ and $5\tilde{\sigma}$ orbitals reverse polarization and strengthen the internal CO_{ads} bond. The π-σ model does not consider charge donation from the CO regions of the $4\tilde{\sigma}$ and $5\tilde{\sigma}$ orbitals to the substrate bands. *Therefore, the $\tilde{\sigma}$-system is repulsive to the surface.* The internal CO_{ads} bond weakens upon adsorption, because the weakening of the $\tilde{\pi}$-system more than offsets the strengthening of the $\tilde{\sigma}$-system.

Dimakis-Smotkin extended π-σ model: The extended π-σ model considers the same $\tilde{\pi}$-system as does the π-σ model: The $d_{\tilde{\pi}}$- and $2\tilde{\pi}^*$-bands are equivalent to the π-σ model $d_{\tilde{\pi}}$-lower energy region and $d_{\tilde{\pi}}$-higher energy region, respectively. The innovation of this model is inclusion of the

4

interactive components of the $\tilde{\sigma}$-system orbitals/bands via donation from the $4\tilde{\sigma}$ and $5\tilde{\sigma}$ orbitals to the substrate bands. In the extended π-σ model, the $\tilde{\sigma}$-system is C-Metal bonding. The C-Metal $4\tilde{\sigma}$ and $5\tilde{\sigma}$ bonding orbitals are not offset by the antibonding $d_{\tilde{\sigma}}$-band. This was not the case in the original π-σ model, which assumed all $\tilde{\sigma}$-system orbitals/bands below the Fermi level were filled (Ref. 11). Incomplete occupancy of the $d_{\tilde{\sigma}}$-band was confirmed by Rangelov et al., using inverse photoemission spectra of CO/Ni, CO/Pd, and CO/Pt. [24] In the extended π-σ model, the effect of the $5\tilde{\sigma}$ orbital on the internal CO_{ads} bond is small.[14] The extended π-σ model has been used by other research groups.[25-28]

We described an expression that correlates changes in v_{CO} to changes in the CO_{ads}, C and O atomic orbital charges (Ref. 17). Here we modify the expression for v_{CO} from our prior report by including the oxygen contribution to the $2\tilde{\pi}^*$-band as,

$$v_{CO} \propto -(Q_{O2s}^{4\tilde{\sigma}} + Q_{C2s}^{5\tilde{\sigma}} + Q_{C2s}^{d_{\tilde{\sigma}}} + Q_{Cpxy}^{\tilde{\pi}} + Q_{Opxy}^{\widetilde{2\pi^*}}) \quad (1)$$

where Q_y^x are charge contributions of the *y* atomic orbital to the *x* tilde-type orbital/band. This expression improves the description of the $\tilde{\pi}$-system, by allowing for charge to be directly transferred between CO_{ads} and interacting water molecules.

1.2. Quantum theory of atoms in molecules (QTAIM) applied to CO adsorbed on metals

Phenomenological models based on adsorbate orbital occupation have shortcomings. Orbital charges, obtained by integration of densities-of-states (DOS) spectra, do not always correlate to bond strengths. Bader and co-workers have developed the quantum theory of atoms in molecules (QTAIM), which is based on the topology of $\rho(\vec{r})$, $\nabla\rho(\vec{r})$, and the Laplacian $\nabla^2\rho(\vec{r})$ to describe atoms and bonds of chemical systems. QTAIM analyses are basis set and method independent, as long as a minimally adequate basis set is used.[29] Fig. 1 shows the free CO $\rho(\vec{r})$ and the $\nabla\rho(\vec{r})$ associated with the CO bond critical point. It also shows the negative of the

Laplacian $-\nabla^2\rho(\vec{r})$ associated with the oxygen and carbon non-bonding charge concentrations (i.e., presence of lone pair electrons). The 2D $\rho(\vec{r})$ and $-\nabla^2\rho(\vec{r})$ are plotted with CRYSPLOT.[30] The AIM-UC program was used to plot and calculate the 3D $\rho(\vec{r})$ and $-\nabla^2\rho(\vec{r})$ and the $\nabla\rho(\vec{r})$.[31] A pair of atoms are considered "bonded", when a point of zero-flux density (Fig. 1b, black line) along the path connecting these two atoms (bond path) carries charge accumulation in the plane perpendicular to the internuclear axis (Fig. 1a). This point is the bond critical point (saddle point in the 3D $\rho(\vec{r})$). Moreover, the $-\nabla^2\rho(\vec{r})$ is used to determine change accumulation at non-nuclear locations, as in the case of free CO (Fig. 1c). Fig. 1b shows the atomic basins for carbon and oxygen atoms, which are the regions of space traversed by all $\nabla\rho(\vec{r})$ that terminate at the attractor or nucleus and are bounded by zero-flux surfaces.[32]

CO adsorption on metals has been analyzed by QTAIM. [33-38] Macchi and Sironi analyzed CO_{ads} on B, Cr, Fe, Co, Ni, and Cu using transition metal-carbonyl clusters (Ref. 38) and emphasized the difficulty of detecting π^*-backdonation due to $\rho(\vec{r})$ cylindrical symmetry for metal-C bonds. However, they did not relate the non-zero eigenvalues of the $\rho(\vec{r})$ Hessian to 5σ-donation and $2\pi^*$-backdonation between the CO and the adsorbing metal.

Chemical interactions are also described by Energy Decomposition Analysis (EDA),[39,40] Constrained Space Orbital Variation (CSOV),[41,42] Natural Energy Decomposition Analysis-NEDA,[43, 44,45] localized molecular orbitals EDA,[46, 47] and more recently periodic energy decomposition analysis (pEDA).[48] EDA has been extended to the study of CO_{ads} on metals and metal oxides of Li and Na (Ref. 49), Ni (Ref. 11), Cu (Ref. 11, 49, 50), Al (Ref. 56), Pt (Ref. 22, 51), and MgO,[52, 53] where interactions are decomposed into σ and π contributions.

I.g. CO/Pt QTAIM and orbital approach to hydration and CO coverage variations

Here, periodic density functional theory (DFT) [54, 55] is used to model CO/Pt with and without hydration at 1/9, 1/3, and 5/9 monolayer (ML) CO coverages. The internal CO_{ads} and C-
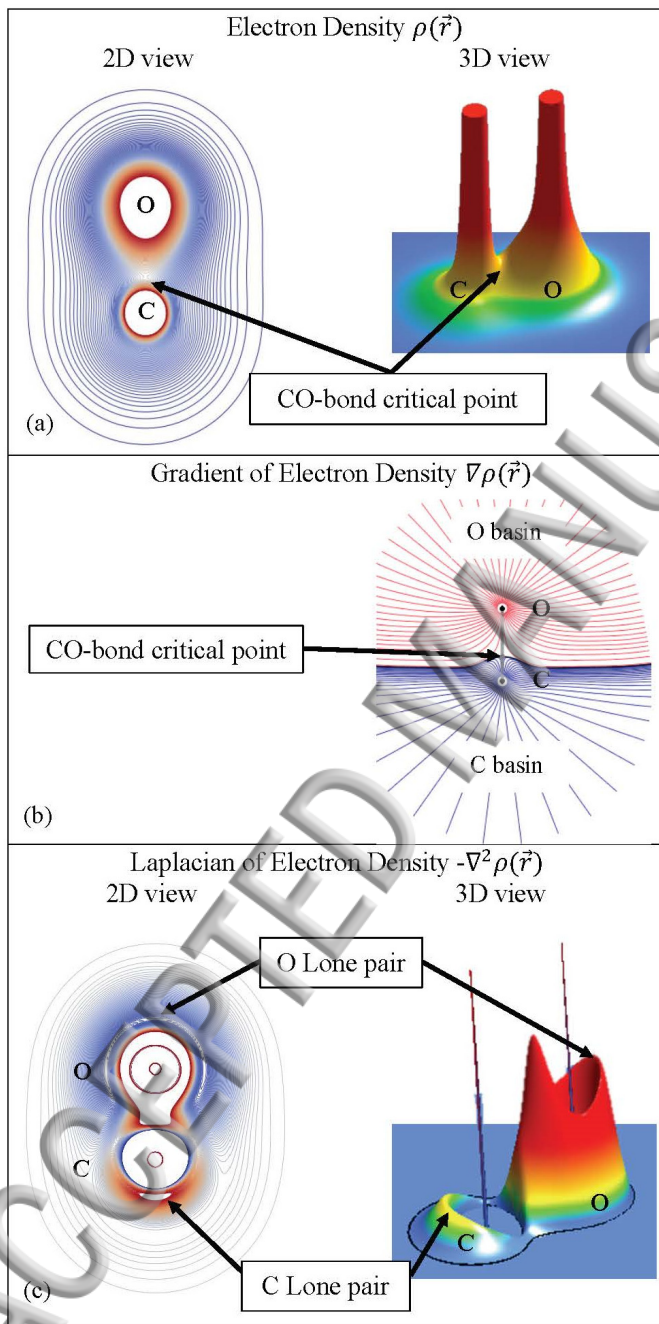

FIG. 1. Free CO representations with labeled bond critical point and lone pairs (a) extrema electron densities $\rho(\vec{r})$: 2D and 3D (high charge, red; low charge, blue); (b) gradient of electron

density $\nabla \rho(\vec{r})$ (oxygen, red; carbon, blue; bond path, gray line; zero flux surface, black line), (c) extrema Laplacian $-\nabla^2 \rho(\vec{r})$: 2D and 3D (color code same as (a)).

Pt bonds are then examined by: 1) QTAIM analyses of $\rho(\vec{r})$ and $\nabla^2 \rho(\vec{r})$ at C-O and C-Pt bond critical points and 2) CO_{ads} orbital approaches. Bond strengths are corelated to changes in the (ν_{CO} and ν_{CPt}) stretching frequencies, the $\rho(\vec{r})$, $\nabla^2 \rho(\vec{r})$, and to QTAIM expressions (vide infra) at critical points vs. CO and water coverages. Changes in the $\rho(\vec{r})$ Hessian non-zero eigenvalues at C-O and C-Pt bond critical points are directly associated with changes in the $\tilde{\sigma}$- and $\tilde{\pi}$-systems, which are used by the extended π-σ model. We also examine the effect of surface relaxation on the above properties by performing frozen and relaxed substrate calculations.

2. STRUCTURES AND COMPUTATIONAL METHODS

2.1. Modelling of the periodic structures

The Pt substrates were modelled as three-layer fcc (111) periodic slabs with 9 atoms per layer in the unit cell. Fig. 2 shows the Pt substrate unit cells, employed in this work, with CO_{ads} at 1/9 and 5/9 ML coverages, with and without interacting water molecules. The C and O atom Mulliken charges[56] (Fig. 2) were calculated using relaxed-top substrate layer configurations. The measured Pt lattice parameter of 3.924 Å was used for the calculations performed with 1) all Pt atoms locked at crystallographic lattice positions (frozen substrate calculations), 2) the top substrate layer relaxed, and 3) both the top and the middle layers relaxed (relaxed substrate calculations). In the latter case, 4 of 9 middle layer atoms were constrained to move only perpendicular to the substrate surface to avoid possible alignment of all three layers (i.e., no longer fcc).

At 1/9 and 1/3 ML coverages, the CO_{ads} were placed atop as (3×3)-CO and (3×3)-3CO overlayers respectively, to the fcc lattice and were free to move during geometry optimization. At

1/9 ML coverage, the atop CO$_{ads}$ were located at the corners of an equilateral triangle. At low

coverages, the CO $_{ads}$ are experimentally observed as atop.[57-62] The frozen substrate calculations

show the atop is preferred by ~ 0.04 eV relative to the three-fold site. However, the relaxed
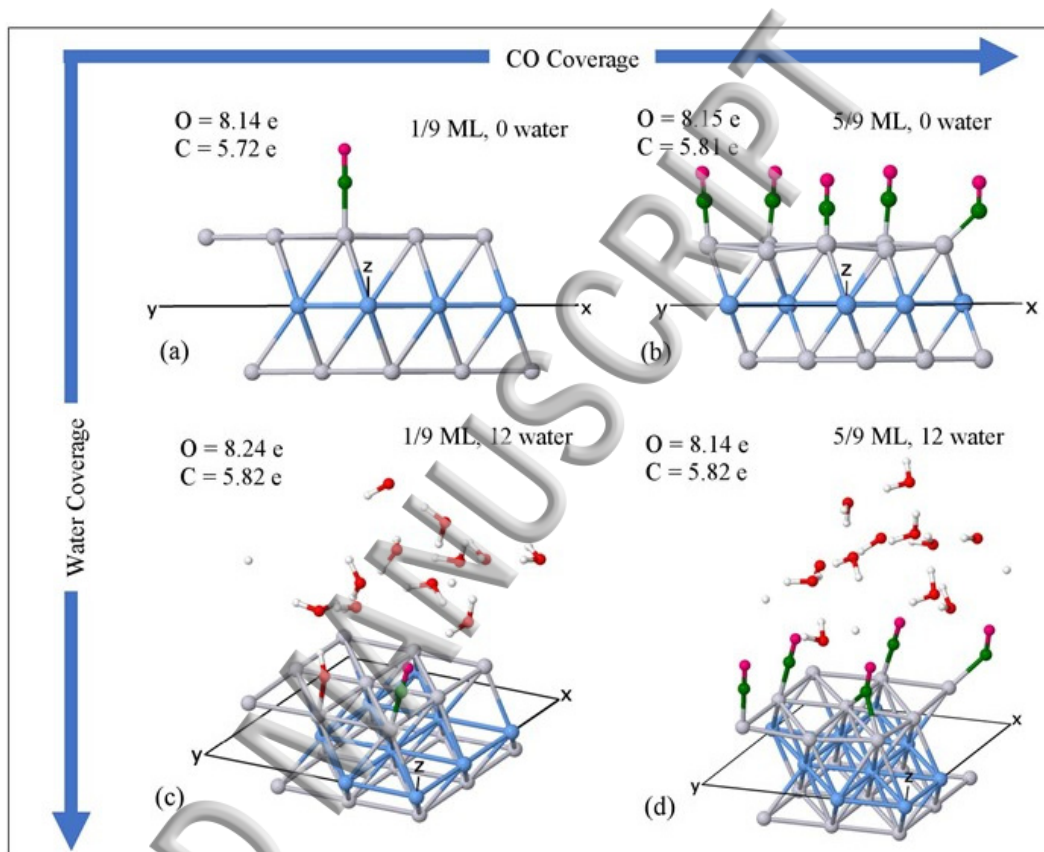

FIG. 2. Unit cells of DFT optimized three-layer Pt slabs, plotted by Jmol,[63] and C and O Mulliken charges on Pt substrate top layer (a) at 1/9 ML and (b) 5/9 ML CO coverages on dry Pt and (c) and (d) corresponding calculations of (a) and (b), respectively by including 12 interacting water molecules. Atoms are colors: Pt (top and bottom layers), gray; Pt (middle layer), light blue; C, green; O (CO$_{ads}$) violet; O (water), red; and H, white.

substrate calculations show the opposite by ~ 0.1 eV. Feibelman et al., using a variety of DFT

codes, found that DFT favors high coordination sites for CO/Pt(111) at low CO coverages,

contrary to experiments. This DFT failure is often referred as the "CO adsorption puzzle".[64] In

In order to reconcile modelling results with experimental observables, the CO molecules are initially positioned atop for 1/9 ML and 1/3 ML coverages. At 5/9 ML CO coverage, five CO are initially placed over the 9-atom Pt surface as follows: three atop, one bridge, and one 3-fold site CO.

At 1/9 ML CO coverage, the $(CO+n*H_2O)/Pt$, $n \leq 12$ optimized geometries were obtained as follows: For $n = 1$, a single water molecule is placed distantly from a geometry optimized CO/Pt. This $(CO+H_2O)/Pt$ initial guess is re-optimized. For $n = 2$, a single water molecule is placed distantly from a geometry optimized $(CO+H_2O)/Pt$, followed by $(CO+2H_2O)/Pt$ re-optimization. The process is repeated for all $(CO+n*H_2O)/Pt$, $n \leq 12$. Alternate methods to develop the series of geometry optimized solvated structures consistently yielded higher conformation energies than our systematic sequential re-optimization approach, ensuring that our optimized geometries are at a global energy minimum. For the 1/3 and 5/9 ML CO coverages, SCF energy convergence was not possible with a water molecule co-adsorbed on the Pt surface. In these cases, the $(CO+12*H_2O)/Pt$ (at the 1/9 ML CO coverage) served as an initial guess followed by separation of the water molecule (co-adsorbed with CO) from the Pt surface and its repositioning distant from the remaining water molecules.

At 1/9 ML CO, calculations used optimized geometries of $(CO+n*H_2O)/Pt$, $n \leq 12$, at frozen, relaxed top, and relaxed top and second layer Pt. At higher coverages, we used relaxed Pt top layer and relaxed top and second layer Pt for calculation of CO/Pt and $CO+12*H_2O/Pt$.

2.2. DFT functional, basis sets, and parameters

Electronic, structural, and vibrational properties of CO_{ads} on dry and hydrated Pt were calculated using the CRYSTAL14 DFT code[65, 66] with Gaussian basis sets centered at the atoms. The PBE0 non-empirical/parameter-free functional was used.[67, 68] The ν_{CO} and ν_{CPt} were

10

calculated at the Γ point $(\vec{k} = \vec{0})$ within the harmonic approximation[69] using a partial Hessian approach for the CO_{ads}. The innermost Pt orbitals were described by Stuttgart-Dresden effective core potentials (ECP),[70, 71] which accounts for mass-velocity and Darwin relativistic corrections. This provides similar accuracy as the all-electron basis sets at a fraction of CPU time. The Pt effective valence basis set [4s4p2d][72] was optimized for crystalline calculations. For C and O, the [4s3p2d] (Ref. 16) basis sets were used, whereas for H, the [3s1p][73] basis set was used. The basis sets were size-limited to avoid linear dependencies, resulting from small exponents present in the Gaussian basis sets. Due to the size of the calculations, Brillouin zone integrations were performed on a 6×6 Monkhorst-Pack grid,[74] whereas the Fermi energy and the density matrix used the 12×12 grid (Gilat grid)[75, 76] without loss of accuracy.

Crystal Orbital Overlap Populations (COOP)[77] were calculated by CRYSTAL14, whereas COOP vs. energy plots were obtained using CRYSTAL17.[78] SCF energy convergence and geometry optimization parameters were described in our past work (Ref. 17). The E_{ads} is given by

$$E_{ads}/n = E_{(n*CO+m*H_2O)/Pt} - E_{m*H_2O/Pt} - n * E_{CO}, n = 1, 2, ..., \text{and } m = 0, 1, 2 \ldots \text{ (eq. 2)}$$

where n and m are the number of CO and water molecules, respectively. This expression is similar to one used by Stampfl and Scheffler for CO and O co-adsorption on Ru.[79] The E_{ads} is calculated with treatment of the basis set superposition error (BSSE),[80] which arises due to finite size of the crystalline basis sets used. The BSSE error ($\sim$0.1 eV, Ref. 17) is minimized using the counterpoise correction[81] by including "ghost" atoms (i.e., atoms with nuclear charge and electrons removed, but basis set retained) in the fragment SCF energy calculations of the adsorbate-substrate structure.

2.3. QTAIM methodology

The $\rho(\vec{r})$ and $-\nabla^2\rho(\vec{r})$ topological analysis was performed with the TOPOND,[82] which is integrated with CRYSTAL14. The bond critical points are denoted as (3, -1), where 3 stands for the three non-zero eigenvalues of the $\rho(\vec{r})$ Hessian at the critical point and -1 is the summation of

number of positive and negative eigenvalues. For the (3, -1) bond critical point, two $\rho(\vec{r})$ curvatures are negative and one is positive, and $\nabla^2\rho(\vec{r})|_{\vec{r}_{cp}}=\lambda_1+\lambda_2+\lambda_3$, where λ_i (i=1, 2, 3) are the non-zero eigenvalues of the $\rho(\vec{r})$ Hessian. The λ_1 and λ_2 values (< 0) are associated with charge accumulation in the planes perpendicular to the bond path and λ_3 (> 0) with charge accumulation along the bond path. Increased λ_3 is indicative of charge accumulation in the atomic basins and the bond being more ionic (Ref. 83).

We also examine a critical point classified as (3, -3), which denotes $\rho(\vec{r})$ local maxima and may correspond to non-nuclear attractors due to $\rho(\vec{r})$ concentration at this point. These points are explored by $-\nabla^2\rho(\vec{r})$, which exhibits altering shells of charge concentrations and depletions (valence shell charge concentration-VSCC, Ref. 32). The sign of $\nabla^2\rho(\vec{r})$ at the bond critical point can be used to identify the type of the bond and is expected to be negative for covalent and positive for ionic bonds. However, for covalent *polar* bonds (e.g., C-O and C-Pt bonds), $\nabla^2\rho(\vec{r})$ is positive at the bond critical point (Ref. 38). For covalent bonds, an improved description of the bond strength is given by $(H/\rho)(\vec{r})$ at the bond critical point $\vec{r}$, such that $H(\vec{r}) = G(\vec{r}) + V(\vec{r})$, where $G(\vec{r})$ is the positive definite kinetic energy density, and $V(\vec{r})$ is the potential energy density.[37] Gatti stated that adoption of a single QTAIM criterion for bond assessment is challenging.[84] Therefore, we use $\rho(\vec{r})$, $\nabla^2\rho(\vec{r})$, and $(H/\rho)(\vec{r})$ at C-O and C-Pt bond critical points to determine changes in the corresponding bond strengths via QTAIM.

2.4. COOP and COHP calculations

For periodic systems, Ruggiero et al.,[85] implemented an improvement to COOP, called Crystal Orbital Hamilton Population (COHP),[86] and is available in CRYSTAL17. The COHP accurately accounts for bond strengths, by partitioning the band energies (i.e., instead of the electron states) into bonding and antibonding regions. However, both COOP and COHP calculations are basis set

dependent. Grechnev et al.,[87] found that COOP and COHP provide acceptable results, when minimal and localized basis sets are used, whereas high-quality basis sets may introduce artificial large antibonding peaks in the energy region near and below the Fermi level, in both the COOP and COHP spectrums. The C-O COOP and COHP are calculated using the entire basis sets described above, whereas for the C-Pt cases, we removed the s orbital from the carbon outermost sp basis function (outermost carbon sp basis function is replaced by a p function) to avoid overestimation of the antibonding C-Pt COOP/COHP $d_{\tilde{\sigma}}$-band.

3. RESULTS AND DISCUSSION

3.1. Hydration effects for CO/Pt at 1/9 ML CO coverage

C-O and C-Pt bond lengths, stretching frequencies, COOP, and E_{ads}. Fig. 3 shows the changes in the C-O and C-Pt bond lengths, the ν_{CO}, ν_{CPt}, corresponding COOP, and the E_{ads} for CO/Pt (frozen and relaxed top substrates) vs. number of waters in the unit cell. Our calculated ν_{CO} values are in supplementary materials (Table SI). At low (1/9 ML) CO coverage, our ν_{CO} values (dry, 2203$_{frozen}$, 2207$_{relaxed}$ cm^{-1}; hydrated with 12 waters: 2113$_{frozen}$, 2121$_{relaxed}$ cm^{-1}) are 2-6 % higher than that reported by prior computations (dry, 2073-2100 cm^{-1}, Ref. 60, 88-91) and experiments (UHV, 2085-2106 cm^{-1}; electrochemical conditions, 2051-2071 cm^{-1}).[92-94] Our ν_{CPt} values (488$_{frozen}$, 515$_{relaxed}$ cm^{-1}) depend on the number of interacting waters and degree of surface relaxation. Our ν_{CPt} values are close to the value measured under UHV of 480 cm^{-1} at and 0.17 ML CO coverage reported by Steininger et al. (Ref. 60). Our DFT calculations, systematically overestimate ν_{CO} and $|E_{ads}|$ (Ref. 17). Our calculated $|E_{ads}|$ for adsorption on dry (1.77-1.68 eV) and hydrated (1.57-1.50 eV; 12 waters) Pt are within the DFT calculated ranges reported by Steckel et al.[95] The top layer lifts by ~ 0.1 Å, when allowed to relax. This lattice expansion is accompanied by systematic shifts in C-O and C-Pt properties (Fig. 3, squares to circles). This top layer relaxation

exceeds that reported by Doll (0.05 Å) for CO/Pt(111) because they used five-layer Pt (Ref. 72).

The C-O calculated properties (Fig. 3a,c, ν_{CO}, C-O distance, and COOP) are minimally affected upon relaxation of the top layer (blue circles) compared to that of the frozen substrate (red squares).

The negative correlation between bond lengths and stretching frequencies is known as Badger's rule. [96-98] We found Badger's rule applicable to the internal CO_{ads} and C-Pt bonds at low
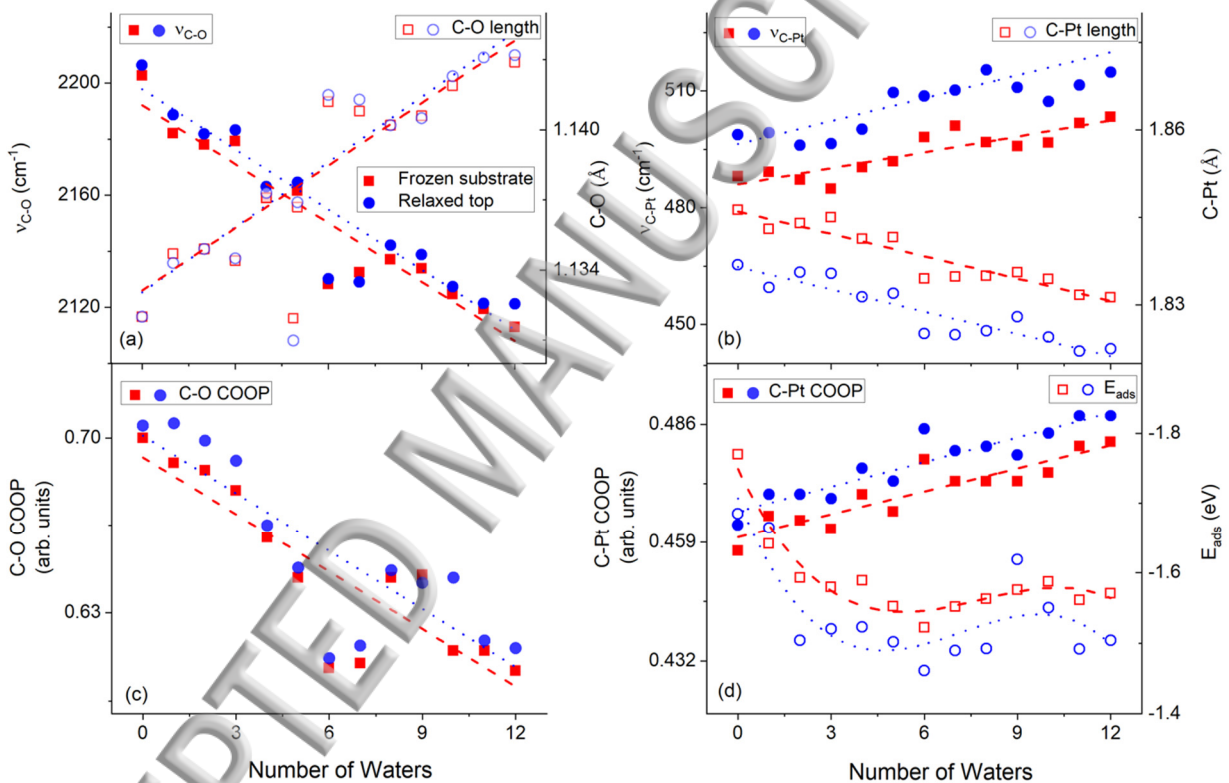
FIG. 3. Frozen (red square) and relaxed top (blue circles) substrate calculations with trend lines (red-dashed and blue-dotted, respectively) for CO/Pt at 1/9 ML CO coverage vs. water molecule number: (a) ν_{CO} and C-O bond lengths, b) ν_{CPt} and C-Pt bond lengths, c) C-O COOP, and d) C-Pt COOP and E_{ads}.

CO coverage, where the C-O bond weakens with hydration. This is confirmed by the ν_{CO} downshift (Fig. 3a, solid), the increase in the C-O bond lengths (Fig. 3a, hollow), and the decrease in the C-

14

COOP (Fig. 3c). The ν_{CO} downshift with hydration is in agreement with infrared reflection absorption spectroscopy (Ref. 93).

At low CO coverage, C-Pt bond strengthening with hydration is verified by the ν_{CPt} upshift (Fig, 3b, solid), the decrease in the C-Pt bond lengths (Fig. 3b, hollow), and the increase in the C-Pt COOP (Fig. 3d). While this does not appear to be consistent with corresponding changes in the E_{ads} (Fig. 3d), the absence of correlation between the C-Metal stretching frequency and the corresponding E_{ads} has been reported (Ref. 14, 17, 89). The C-Metal stretching frequency and E_{ads} are derived from local and global properties of the potential energy surface, respectively: The C-Metal stretching frequency is more closely associated with localized interactions of the adsorbate with the metal atom, whereas the E_{ads} is associated with interactions between the adsorbate and the entire substrate surface. The lack of ν_{CPt} and E_{ads} correlation is attributed to direct charge transfer from water molecules to CO_{ads}. Specifically, for CO_{ads} on hydrated Pt (12 waters), the CO_{ads} charge is increased by ~ 0.19 e (Fig. 2a,c) due to decreases in charges of the adsorbing Pt (0.13 e) and surrounding water molecules (0.06 e).

At low CO coverage, one water molecule is co-adsorbed with CO on the Pt surface (Fig. 2c), whereas this effect is not observed at higher CO coverages (Fig. 2d). As hydration is increased (Fig. 2a-c), electrons are transferred from the water molecules to both the C and O atoms (Fig. 2, Mulliken charges): Thus, the CO contribution to the occupied $2\tilde{\pi}^*$-band increases and leads to C-O bond weakening and C-Pt bond strengthening. At higher CO coverages, deviations from the rule are noticed. Similarly, the observed positive correlation between the COOP and stretching frequencies at low CO coverage is not observed at higher coverages (vide infra).

C-O and C-Pt bond strengths by QTAIM. Fig. 4 shows the values of $\rho(\vec{r})$, $\nabla^2\rho(\vec{r})$, and $|H/\rho(\vec{r})|$ at the C-O and C-Pt bond critical points vs. number of interacting waters and the $\rho(\vec{r})$

Hessian λ_i eigenvalues (i=1, 2, 3) at the C-O and C-Pt bond critical points. The decrease in $\rho(\vec{r})$, $\nabla^2\rho(\vec{r})$, and $|H/\rho(\vec{r})|$ at the C-O bond critical point (Fig. 4a-c, solid), as hydration increases, is indicative of internal CO_{ads} bond weakening. The opposite is observed at the C-Pt bond critical point (Fig. 4a-c, hollow). This agrees with changes from the ν_{CO} and ν_{CPt}, the corresponding bond lengths, and the COOP (Fig. 3). The $\rho(\vec{r})$, $\nabla^2\rho(\vec{r})$, and $|H/\rho(\vec{r})|$ at bond critical points (Fig. 4a-
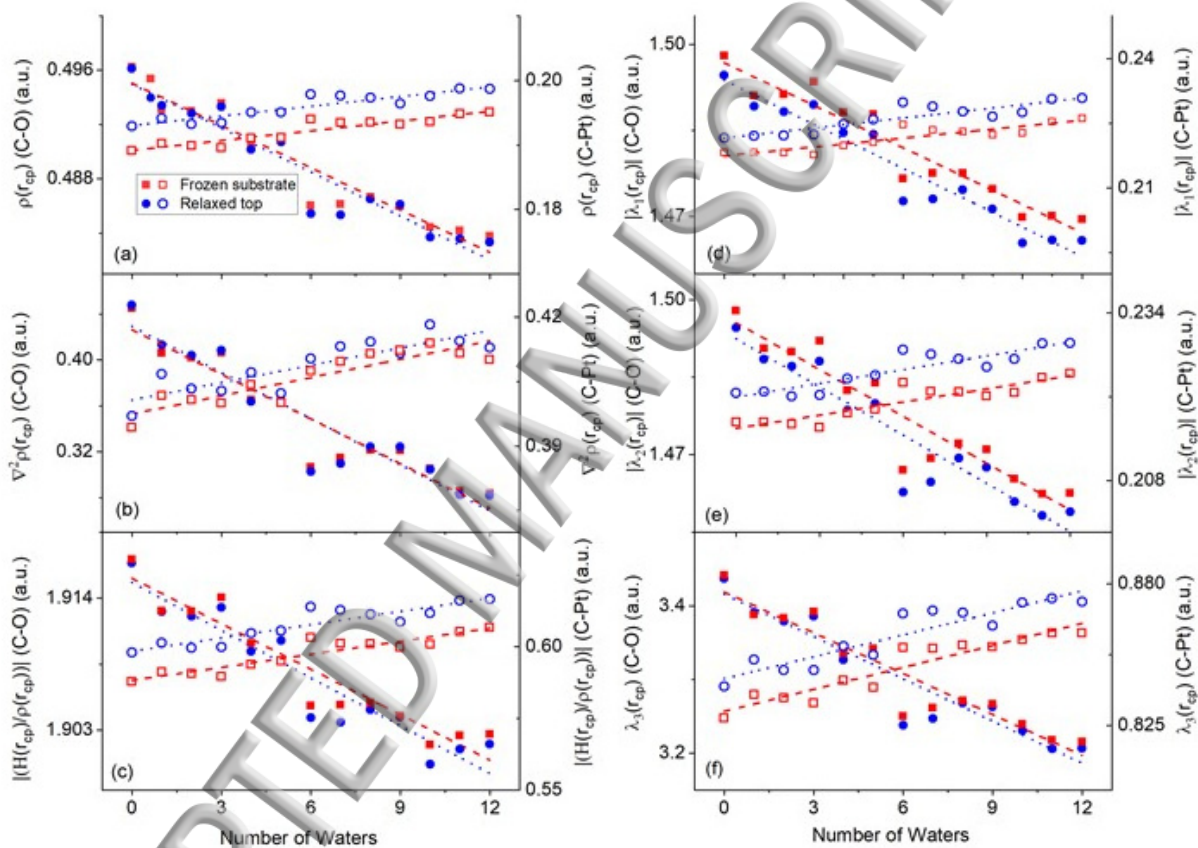
FIG. 4. Frozen (red squares) and relaxed top (blue circles) Pt substrate calculations with trend lines (red-dashed and blue-dotted, respectively) for C-O (solid) and C-Pt (open), a) $\rho(\vec{r})$, (b) $\nabla^2\rho(\vec{r})$, (c) $H/\rho(\vec{r})$, and (d)-(f) $\rho(\vec{r})$ Hessian of the non-zero eigenvalues λ_i (i=1, 2, 3) at the C-O and C-Pt bond critical points relative to the number of interacting water molecules for CO/Pt at 1/9 ML CO coverage.

16

are negatively correlated to changes in the corresponding bond lengths (Fig. 3a and b, hollow) throughout this work. The above QTAIM properties at bond critical points have a positive correlation with corresponding stretching frequencies for all cases except CO_{ads} on dry Pt at CO coverages > 1/9 ML. This will be reconciled in the next section.

Upon hydration, the $|\lambda_i|$ eigenvalues (Fig. 4d-f) at the C-O bond critical point (solid) decrease, while those of the C-Pt bond critical point (hollow) increase. This negative correlation was found for all co-adsorption scenarios involving atop CO_{ads}. The $|\lambda_i|$ eigenvalues positive correlations to the $\rho(\vec{r})$, $\nabla^2\rho(\vec{r})$, and $|H/\rho(\vec{r})|$ at the C-O and C-Pt bond critical points are observed for all adsorptions and coverages. We confirm a positive correlation of $|\lambda_1|$ and $|\lambda_2|$ eigenvalues to C-O π bonding and the same for λ_3 values to C-O σ bonding (vide infra).

Fig. 5 shows the oxygen to C-O-bond-critical-point distance (R_{O-bcp}) from the $\rho(\vec{r})$ (Fig. 5a-b) and the carbon (3, -3) non-bonding VSCC $-\nabla^2\rho(\vec{r})$ $|\lambda_3|$ eigenvalue (Fig. 5c-d) vs. water number for 1/9 ML CO_{ads} on Pt. The increase of R_{O-bcp} with hydration (Fig. 5b) is consistent with internal CO_{ads} bond weakening and increased CO contribution to the C-O antibonding $2\tilde{\pi}^*$-band (Ref. 38). The (3, -3) carbon VSCC $|\lambda_3|$ eigenvalue (Fig. 5d) decreases with hydration, suggesting a decrease in the carbon non-bonding $\rho(\vec{r})$ along the C-Pt axis. The C-Pt bond critical point λ_3 eigenvalue increases (Fig. 4f) with hydration, suggesting that the C-Pt $\tilde{\sigma}$-system becomes more ionic (i.e., charge is concentrated in the C and Pt basins).

C-O and C-Pt overlap populations and phenomenological models. The relationship between internal CO_{ads} and C-Pt bond strengths to surface hydration were correlated to C-O and C-Pt overlap populations. Moreover, these changes in bond strengths are predicted by the 5σ donation-$2\pi^*$ backdonation and extended π-σ models. Fig. 6 shows the DOS, COOP, and COHP spectra at 1/9 ML CO coverage with the top Pt layer relaxed, with and without 12 interacting water

molecules. Positive and negative COOP denote bonding and antibonding (i.e., extent of bonding), respectively. The -COHP is equivalent to COOP, thus COOP and -COHP predict extent of bonding (i.e., COOP gives bond order; -COHP gives bond strength, Ref. 78).

The COOP and -COHP (Fig. 6c-f) confirm the C-O and C-Pt extent of bonding in terms of the $\tilde{\sigma}$- and $\tilde{\pi}$-systems orbitals/bands, described in the introduction. Hydration shifts the $4\tilde{\sigma}$ and $5\tilde{\sigma}$ orbitals towards more negative energies and broadens the $5\tilde{\sigma}$ orbital as seen by the DOS, COOP,
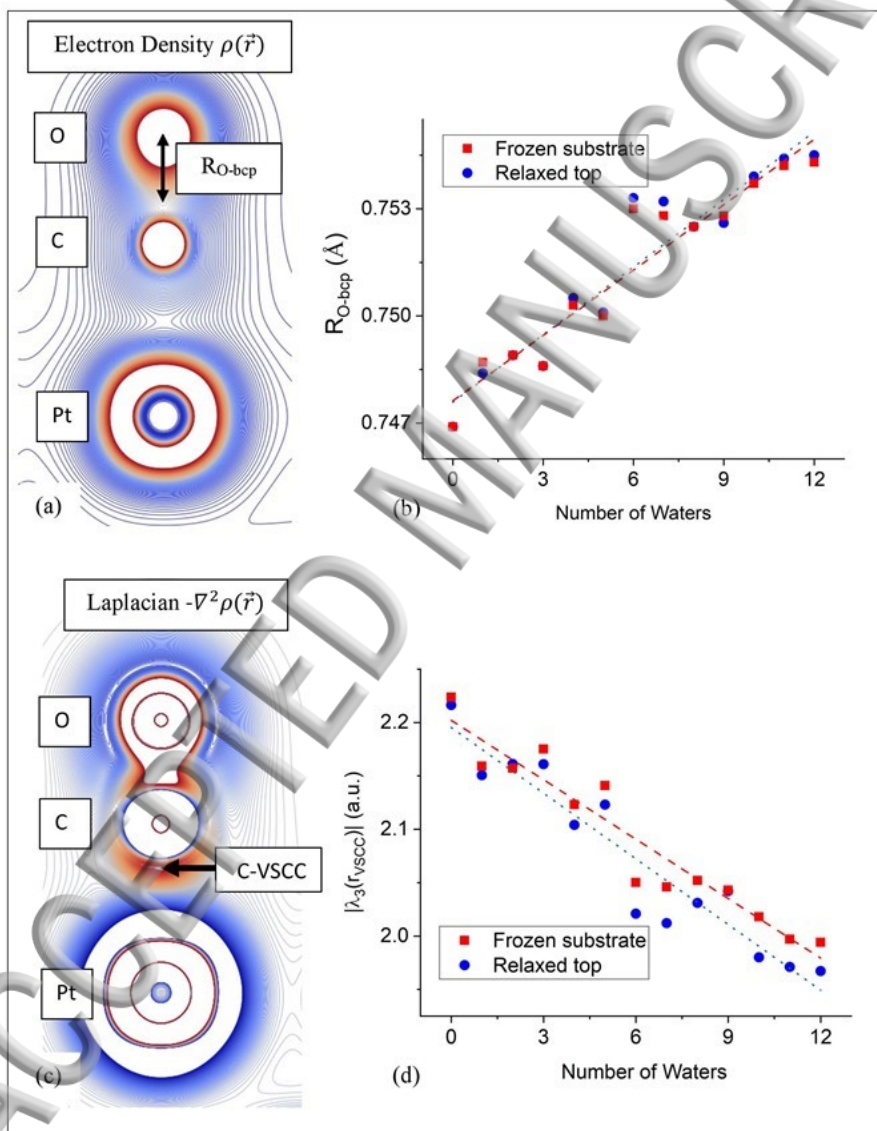

FIG. 5. QTAIM calculated properties for CO_{ads} on Pt at 1/9 ML CO coverage at varied hydration: (a) extrema electron density $\rho(\vec{r})$ (dry case: high charge, red; low charge, blue), (b) distance from

oxygen to the C-O bond critical point (R_{O-bcp}) vs waters number, c) extrema Laplacian $-\nabla^2 \rho(\vec{r})$ (dry case: high charge, red; low charge, blue), and d) carbon non-bonding valence shell charge concentration (VSCC, (3, -3)) $|\lambda_3|$ value vs. waters number.

and COHP spectra (Fig. 6a,c,e). For dry (Fig. 6e, solid red) and hydrated (Fig. 6e, dotted red, 12 waters) CO/Pt, the $5\tilde{\sigma}$ C-O strengths, given by -COHP, are about 40 % (dry) and 10 % (hydrated)
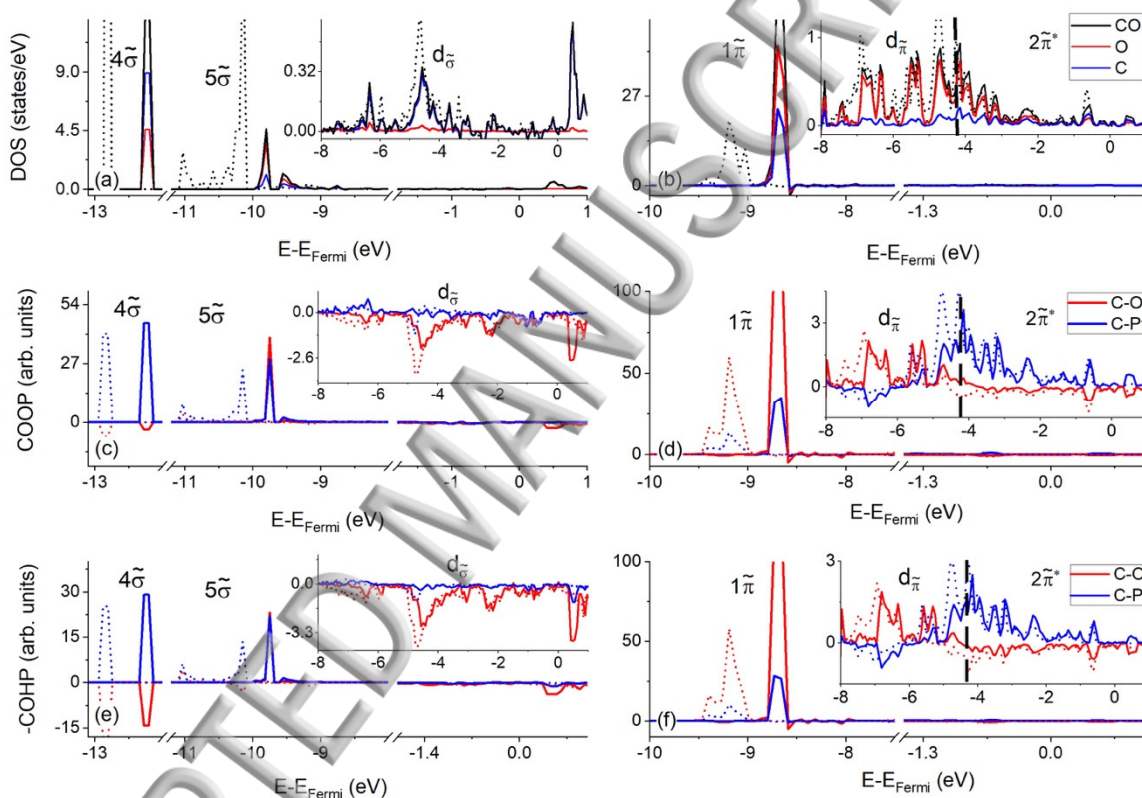
FIG. 6. DFT calculated spectra of CO_{ads} on dry (solid) and hydrated (dotted;12 waters) Pt at 1/9 ML CO coverage with a relaxed top Pt substrate layer: (a)-(b), DOS (black, CO; red, O; blue, C), (c)-(d), COOP (red, C-O; blue, C-Pt), and (e)-(f) -COHP (red, C-O; blue, C-Pt). Vertical dashed black lines, $d_{\tilde{\pi}}$- and $2\tilde{\pi}^*$- energy bands region separation.

of comparable $4\tilde{\sigma}$ strengths: The -COHP (and COOP) spectra integrations show that hydration enhances the $4\tilde{\sigma}$ C-O antibonding character and diminishes the $5\tilde{\sigma}$ C-O bonding character.

Moreover, the COOP and -COHP show that changes in the $d_{\tilde{\sigma}}$-band upon hydration further weaken the internal CO_{ads} bond (Fig. 6c,e inserts, solid and dotted red lines). The DOS shows that the $4\tilde{\sigma}$ orbital is polarized towards carbon, whereas the $5\tilde{\sigma}$ orbital is polarized towards oxygen (Fig. 6a, blue and red solid lines). These polarizations are opposite to those of the free CO 4σ and 5σ molecular orbitals, in agreement with past reports (Ref. 10-14, 17, 23).

Hydration downshifts and broadens all $\tilde{\pi}$-system orbital/bands (Fig. 6b,d,f). This decreases the C-O $1\tilde{\pi}$ orbital bonding and substantially increases the $2\tilde{\pi}^*$ antibonding, whereas the $d_{\tilde{\pi}}$-band remains relatively unchanged (Fig. 6f, solid and dotted red lines integrations), in agreement with changes in the orbitals/bands CO contributions, shown by DOS integrations. The DOS, COOP, and -COHP show that the $\tilde{\sigma}$- and $\tilde{\pi}$-systems weaken the internal CO_{ads} bond upon hydration. The COOP and the -COHP spectra facilitate the selection of the $d_{\tilde{\pi}}$- and $2\tilde{\pi}^*$-bands energy regions for calculation of corresponding CO contributions used in phenomenological models.

Fig. 7 shows charge differences between C and O for the $4\tilde{\sigma}$ and $5\tilde{\sigma}$ orbitals, the CO contributions to the $1\tilde{\pi} + d_{\tilde{\pi}}$, the $2\tilde{\pi}^*$-band, and the $\tilde{\sigma}$- and $\tilde{\pi}$-systems, as well as the 5σ donation-$2\pi^*$ backdonation model and the extended π-σ model (eq. 1) relative to the number of interacting waters (relaxed top substrate calculations). Hydration decreases both the $4\tilde{\sigma}$ and $5\tilde{\sigma}$ polarizations towards carbon and the oxygen, respectively (Fig. 7a), and increases the CO contributions to the $\tilde{\sigma}$-system (Fig. 7c, solid circle and Fig. S1). These effects weaken the internal CO_{ads} and C-Pt bonds.

The overall decreased CO contribution to the $\tilde{\pi}$-system upon hydration, weakens the internal CO_{ads} bond (Fig. 7b, hollow circles). This is attributed to increased CO charges in the C-O antibonding $2\tilde{\pi}^*$-band (Fig. 7b, solid circles) and decreases in the net CO contribution to the $1\tilde{\pi}$ orbital and the $d_{\tilde{\pi}}$-band, both being C-O bonding (Fig. 7b, hollow circles). The overall

strengthening of the C-Pt bond is due to a competition between the C-Pt $\tilde{\sigma}$- and the $\tilde{\pi}$-systems. More specifically, hydration enhances C-Pt antibonding, via changes in the $\tilde{\sigma}$-system, and increases C-Pt bonding, via changes in the $\tilde{\pi}$-system. Both phenomenological models predict weakening of the internal CO_{ads} bond, along with increased hydration (Fig. 7d). However, the agreement of the 5σ donation-2π* backdonation model in the weakening of the internal CO_{ads} bond
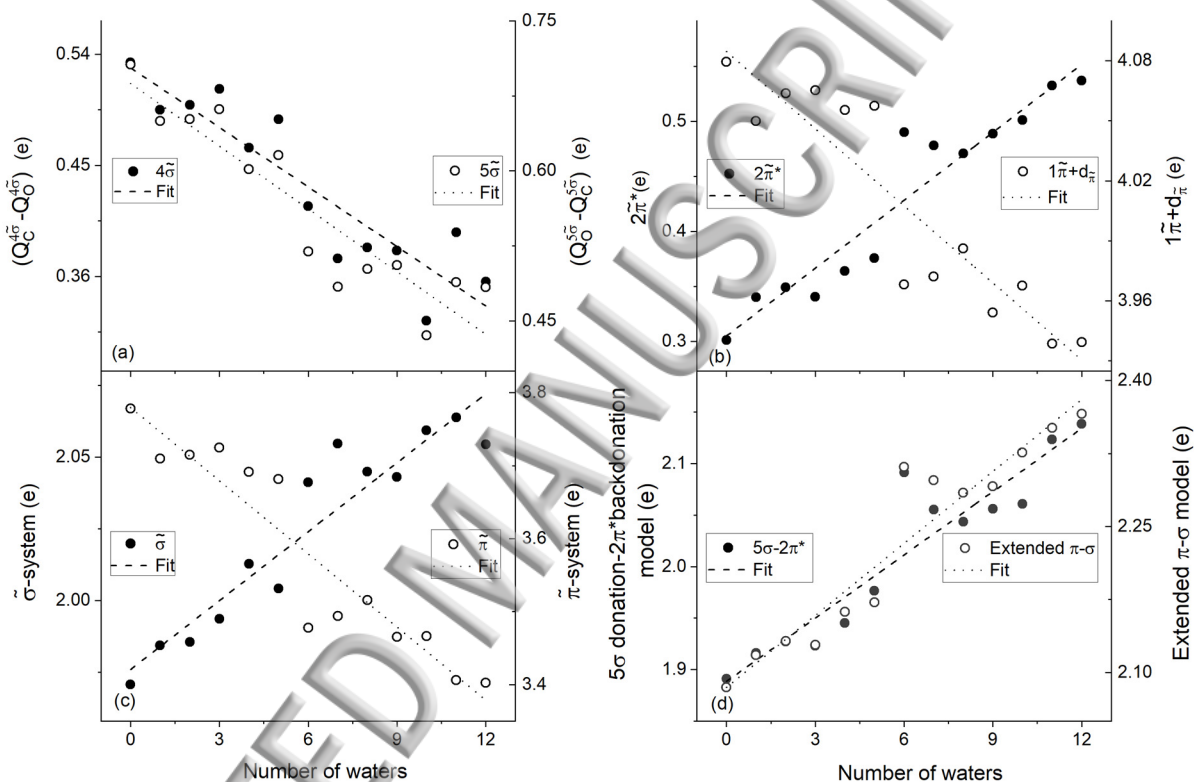
FIG. 7. (a) Charge differences between C and O for the CO/Pt at 1/9 ML CO coverage, calculated by relaxing the Pt substrate top layer relative to the number of interacting water molecules for $4\tilde{\sigma}$ and $5\tilde{\sigma}$ orbitals. The CO contributions to the (b) $1\tilde{\pi}$ and $d_{\tilde{\pi}}$-band and the $2\tilde{\pi}^*$-band and (c) the $\tilde{\sigma}$- and $\tilde{\pi}$-systems. Outputs from (d) 5σ donation-2π* backdonation model and the π-σ model (eq. 1). The CO contributions to the $\tilde{\sigma}$-system do not include the $5\tilde{\sigma}$ orbital.

is fortuitous. The 5σ donation-2π* backdonation model uses the free CO 5σ and 2π* molecular orbitals charges (C-O antibonding) to estimate the internal CO_{ads} bond strength. At low CO

coverage, the 5σ charge is constant upon hydration and, thus the weakening of the internal CO_{ads} bond is only due to increases in the 2π* charge (i.e., single parameter model).

QTAIM and orbital analyses comparison. For CO_{atop} at 1/9 ML coverage, QTAIM and phenomenological models show the internal C-O bond weakens, while the C-Pt bonds strengthens (via competition between $\tilde{\sigma}$- and system $\tilde{\pi}$-systems) with hydration. The decreased C-O critical point $|\lambda_1|$ and $|\lambda_2|$ eigenvalues (Fig. 4d,e) and increases in R_{O-bcp} values (Fig. 5b) correspond to weaker C-O π bonding. Moreover, the decreased λ_3 eigenvalue at the C-O critical point (Fig. 4f) corresponds to a weaker C-O σ bonding.

3.2. CO coverage effect for adsorption on dry and hydrated Pt

C-O and C-Pt stretching frequency and bond length coverage dependence. We quantified effects of CO coverage and hydration on atop internal C-O and C-Pt bond strengths by QTAIM and adsorbate orbital analyses as described above. Figure 8 shows the variation of ν_{CO} and ν_{CPt}, bond lengths, COOP, and the E_{ads} (on dry and hydrated Pt) with coverage at 1/9 ML, 1/3 ML, and 5/9 ML. The ν_{CO} upshift with coverage, has been attributed to decreased 2π*-backdonation.[99] Liu et al. explain further that at higher coverages, competition for a finite number of d-band electrons results in a per molecule reduction of 2π*-backdonation (Ref. 92). The ν_{CO} upshift is also a consequence of dipole-dipole (i.e., intermolecular) coupling (Ref. 20, 99-102). Thus, CO intermolecular coupling serves as a probe for CO island formation (Ref. 93, 103, 104). Our ν_{CO} values are upshifted along with the increased CO coverage by about 13 cm^{-1} and 97 cm^{-1}, for adsorption on dry and hydrated Pt, respectively (Fig 8b). In the latter case, the substantial ν_{CO} upshift is mostly between the CO/Pt configurations at 1/9 ML and 1/3 ML CO to the coverages and is attributed to the water-CO co-adsorption that appears at the low CO coverage but is absent at higher coverages (Fig. 2c). Moreover, these ν_{CO} upshifts are accompanied by decreases in the

C-O bond lengths (Fig. 8a), in agreement with Badger's rule (i.e., negative correlation between bond lengths and stretching frequencies, Ref. 96-98).

In the absence of hydration, the correlations between changes in the C-O distances and ν_{CO}, as the CO coverage varies (Fig. 8a,b), do not adhere to Badger's rule (i.e., not negatively correlated). For these cases, the internal CO_{ads} bond strength, predicted by the QTAIM properties $\rho(\vec{r})$, $\nabla^2\rho(\vec{r})$, and $|H/\rho(\vec{r})|$ at the C-O bond critical point, is near constant between 1/9 ML and 5/9 ML CO coverages, in contrast with ν_{CO} upshifting (vide infra). The ν_{CO} upshift with increasing CO coverage, Fig. 8b) is consistent with past reports for adsorption on hydrated (Ref. 92) and dry Pt (Ref. 16, 90, 91, 95, 105-107), and is consistent with internal CO_{ads} bond strengthening.

Similar to our past report for CO_{ads} on Pt and Ru surfaces, at high CO coverages, changes in the C-O and C-Pt COOP (Fig. 8c, f) do not correlate with changes in the ν_{CO} and ν_{CPt} (Fig. 8b,e), respectively (Ref. 16). Negative correlations between COOP and corresponding stretching frequencies for adsorption on dry Pt have been attributed to hybridization defects (Ref. 17). Kaupp et al. reported that shorter bonds are not necessarily stronger bonds, due to possible sp hybridization defects, where the s orbital may have insufficient charge to hybridize with the p orbital.[108] Increased CO coverage, from 1/9 ML to 5/9 ML, weakens the C-Pt bond, as verified by the downshifts of the ν_{CPt} (averaged between the two relaxed substrate calculations, Fig. 8e) and the increases in the C-Pt distances (Fig. 8d). The weakening of the C-Pt bond with increased CO coverage is more pronounced with hydration. Concomitantly, for adsorption on dry Pt, the E_{ads} becomes less negative, in agreement with past reports (Fig. 8f, blue lines and symbols and Ref. 16). Whereas, when water is present, the 1/9 ML and 5/9 ML CO coverage E_{ads} are about the same and are significantly more negative at the 1/3 ML coverage (Fig. 8f, gray lines and symbols). As

in the last section, there is no general trend between the ν_{CPt} and E$_{ads}$ and this is also found in the next sections.

QTAIM and phenomenological models. Fig. 9 show the QTAIM properties $\rho(\vec{r})$, $\nabla^2\rho(\vec{r})$, and $|H/\rho(\vec{r})|$ at the C-O and C-Pt bond critical points, at various CO coverages for atop adsorption on dry and hydrated Pt. Corresponding changes in the $|\lambda_i|$ (i=1, 2, 3) eigenvalues are shown in Fig. S2 and follow the same pattern as the Fig. 8 QTAIM properties. The values of these properties at the C-O and C-Pt bond critical points reveal some noteworthy differences for the strength of the corresponding bonds between adsorption on dry and hydrated Pt, as CO coverage
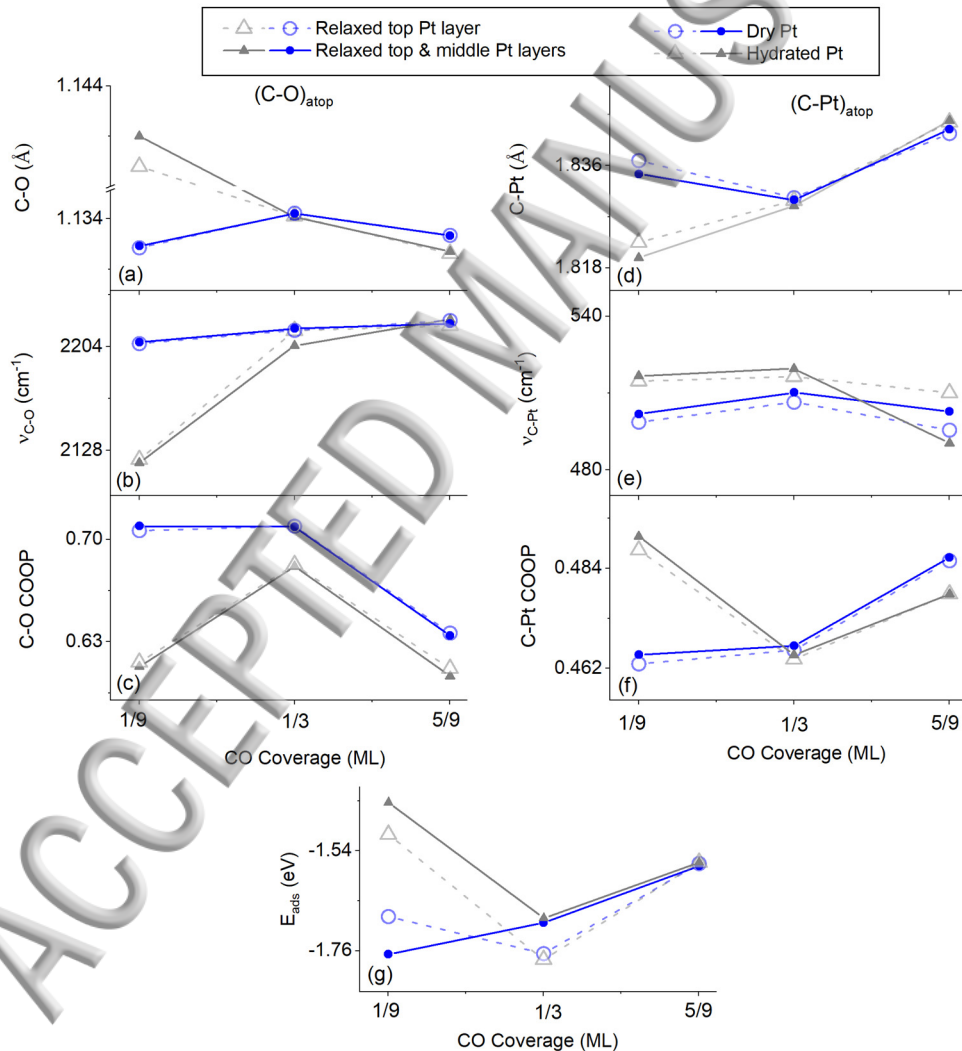
FIG. 8. DFT calculated properties vs. CO atop coverage on dry (blue circles) and hydrated (gray triangles, 12 water) Pt. Relaxed top substrate layer (hollow shapes); Both top and middle substrate layers relaxed (solid shapes): (a) C-O bond length, (b) CO ν_{CO}, (c) C-O COOP, (d) C-Pt bond length, (e) ν_{CPt}, (f) C-Pt COOP, and (g) C-Pt COOP and E_{ads}.

increases. More specifically, for adsorption on dry Pt, the predicted QTAIM internal CO_{ads} bond strengths do not correlate with changes in the ν_{CO} and follow the trends shown in Fig. 9. However, for adsorption on hydrated Pt, QTAIM shows internal CO_{ads} bond strengthen and C-Pt bond weaken, along with increased CO coverage, and are in agreement with changes in the ν_{CO} and ν_{CPt}.

Table I shows the CO contributions to the tilde-type orbital/bands, and outputs from the 5σ donation-$2\pi^*$ backdonation and extended π-σ models for CO/Pt at various coverages, with and without hydration (in units of e). For adsorption on hydrated Pt, increased CO coverage, strengthens the C-O $\tilde{\pi}$-system (Table I, $1\tilde{\pi} + d_{\tilde{\pi}} - 2\tilde{\pi}^*$ values). Additional calculations show that increased CO coverage on hydrated Pt increases the $4\tilde{\sigma}$ polarization towards carbon and $5\tilde{\sigma}$ towards oxygen, thus strengthening the CO_{ads} (i.e., stronger C-O $\tilde{\sigma}$-system), whereas there is no clear trend is described from the changes of overall CO contributions to the $\tilde{\sigma}$-system. The combined effect of the charges and polarization changes in C-O $\tilde{\sigma}$-system is described by the changes in the QTAIM λ_3 eigenvalue: Here, the increased λ_3 eigenvalue (at the C-O bond critical point) is indicative of the $\tilde{\sigma}$-system being more bonding.

Fig. 10 shows the $R_{O\text{-}bcp}$ and the $|\lambda_3|$ at the VSCC carbon non-bonding location (3, -3) vs. CO atop adsorption on hydrated and dry Pt at 1/9ML, 1/3ML, and 5/9 ML. Fig. 10b shows that there is no charge change at the carbon non-bonding location along the C-Pt axis between 1/3 ML and 5/9 ML CO coverages. At the 1/9 ML CO coverage, the absence of hydration increases the

$|\lambda_3|$ value at the VSCC carbon non-bonding location, in agreement with the changes in the $\tilde{\sigma}$ system polarization between adsorption on dry and hydrated Pt. At 1/3ML, and 5/9 ML coverages, no significant changes are observed in the $|\lambda_3|$ value at the VSCC carbon non-bonding location.

On hydrated Pt, both the 5σ donation-2π* backdonation and the extended π-σ models show stronger internal CO_{ads} bond with increasing CO coverage (Table 1). These models are consistent with calculated changes in the QTAIM properties at the C-O critical points (Fig. 9a,c,e, gray symbols and lines) and the upshifts of the ν_{CO} (Fig. 8b, gray symbols and lines).
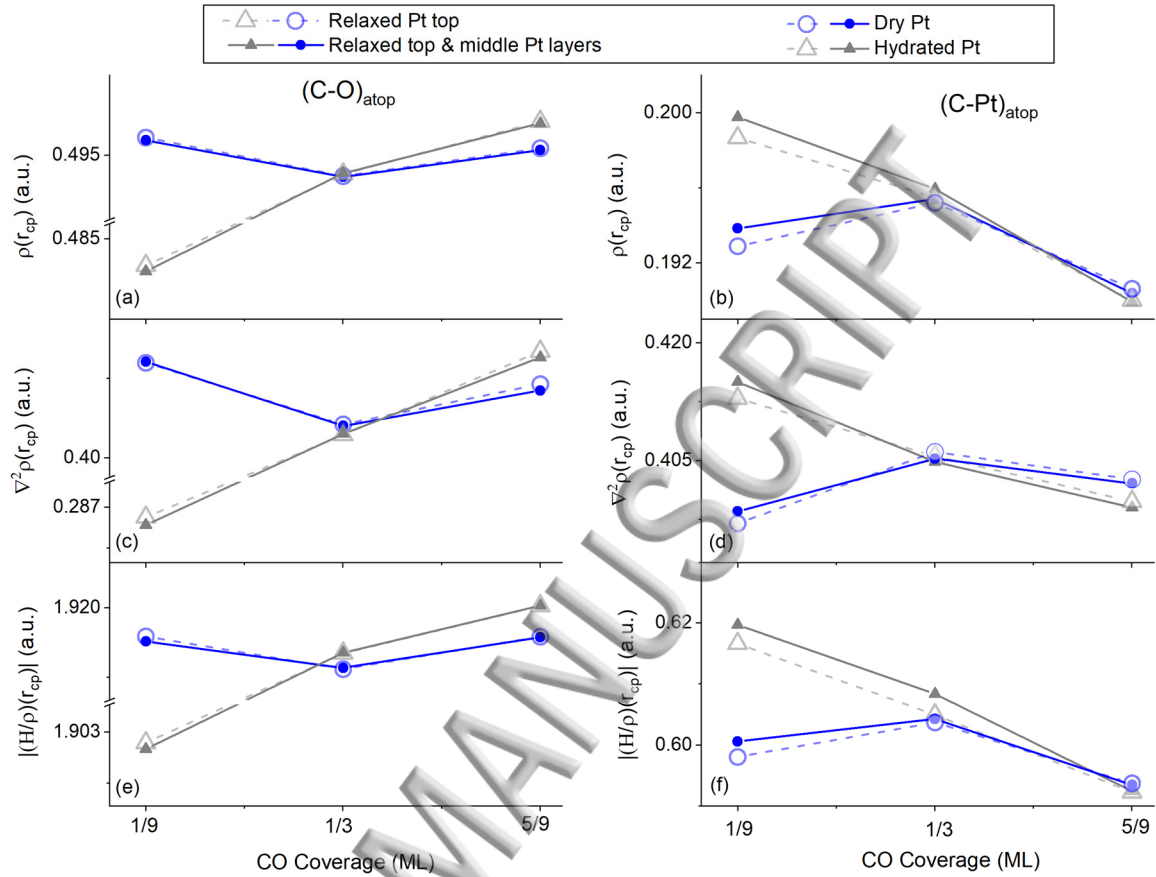
FIG. 9. QTAIM calculated properties at the C-O and C-Pt bond critical points vs. CO atop coverage on dry (blue circles) and hydrated (gray triangles, 12 water) Pt. Relaxed top substrate (hollow shapes); Both top and middle substrate layers relaxed (solid shapes): (a) and (b) $\rho(\vec{r})$, (c) and (d) $\nabla^2\rho(\vec{r})$, and (e) and (f) $H/\rho(\vec{r})$.

However, in the absence of hydration, both models show that the internal CO_{ads} bond strength follows the changes in the C-O COOP (Fig. 8c, blue symbols and lines). We examine the case of increased CO coverage from 1/9 ML to 1/3 ML, where QTAIM properties show internal CO_{ads} bond weaken, in contrast with the ν_{CO} upshift (Fig. 8b, blue symbols and lines). Recall that,

Table I. CO contributions to the tilde-type orbital/bands, and outputs from the 5σ donation-2π* backdonation and extended π-σ models for CO/Pt at 1/9ML, 1/3ML, and 5/9 ML CO coverages with and without 12 interacting waters per unit cell. The Pt top layer was relaxed during geometry optimizations. Values in parenthesis refer to the hydrated case. Rows for the 5/9 ML CO coverage refers to atop, bridge, and 3-fold sites values. The higher values on the both phenomenological models are indicative of weaker internal CO_{ads} bond.

CO Orbital/Band	CO Coverage		
	1/9 ML	1/3 ML	5/9 ML
$4\tilde{\sigma}$	1.653 (1.728)	1.678 (1.671)	1.668 (1.655)
			1.655 (1.643)
			1.763 (1.790)
$5\tilde{\sigma}$	1.590 (1.601)	1.581 (1.582)	1.620 (1.627)
			1.696 (1.683)
			1.700 (1.631)
$d_{\tilde{\sigma}}$	0.317 (0.326)	0.298 (0.322)	0.354 (0.364)
			0.409 (0.423)
			0.507 (0.542)
$1\tilde{\pi}$	3.531 (3.521)	3.559 (3.544)	3.455 (3.489)
			2.850 (2.677)
			2.555 (2.464)
$d_{\tilde{\pi}}$	0.548 (0.419)	0.554 (0.502)	0.611 (0.551)
			1.054 (1.031)
			1.126 (1.337)
$2\tilde{\pi}^*$	0.301 (0.537)	0.285 (0.346)	0.291 (0.280)
			0.800 (0.788)
			0.905 (0.854)
Models			

$5\sigma - 2\pi*$	1.891 (2.138)	1.866 (1.929)	1.912 (1.908)
			2.496 (2.471)
			2.605 (2.486)
Extended π-σ	2.085 (2.366)	2.077 (2.140)	2.122 (2.114)
			2.658 (2.640)
			2.876 (2.830)

in this case, C-O and the ν_{CO} do not follow the Badger rule (Fig. 8a, b). Table I shows that both models predict increased C-O $\tilde{\pi}$-system bonding via decreased $2\pi*$ charge, for adsorption on dry Pt. For the extended π-σ model, increased C-O bonding due to changes in the $\tilde{\pi}$-system more than offsets the C-O bond weakening due to changes in the $\tilde{\sigma}$-system, the latter agreeing with the changes in the QTAIM λ_3 eigenvalue at the C-O bond critical point (Fig. S2c). Therefore, in the absence of a negative correlation between bond lengths and stretching frequencies, phenomenological models that use charge contributions to the adsorbate/molecular orbitals as inputs, are not consistent with QTAIM calculations of the internal CO$_{ads}$ bond strengths. However, the QTAIM non-zero eigenvalues λ_1, λ_2, and λ_3 can serve as substitutes for the adsorbate orbital information since they are directly correlated with changes in the $\tilde{\sigma}$- and $\tilde{\pi}$-systems and their summation is equal to the value of $\nabla^2\rho(\vec{r})$ at the bond critical points. This statement applies to all cases and provides a basis set and method independent approach for C-O and C-Pt bond strength assessment.

3.3. Bridge and 3-fold Pt sites: 5/9 ML CO co-adsorbed with water

The internal CO$_{ads}$ and C-Pt bonds at bridge and 3-fold sites at 5/9 ML CO coverage are contrasted with atop adsorption. Fig. 11 shows changes in the ν_{CO}, ν_{CPt}, the respective bond
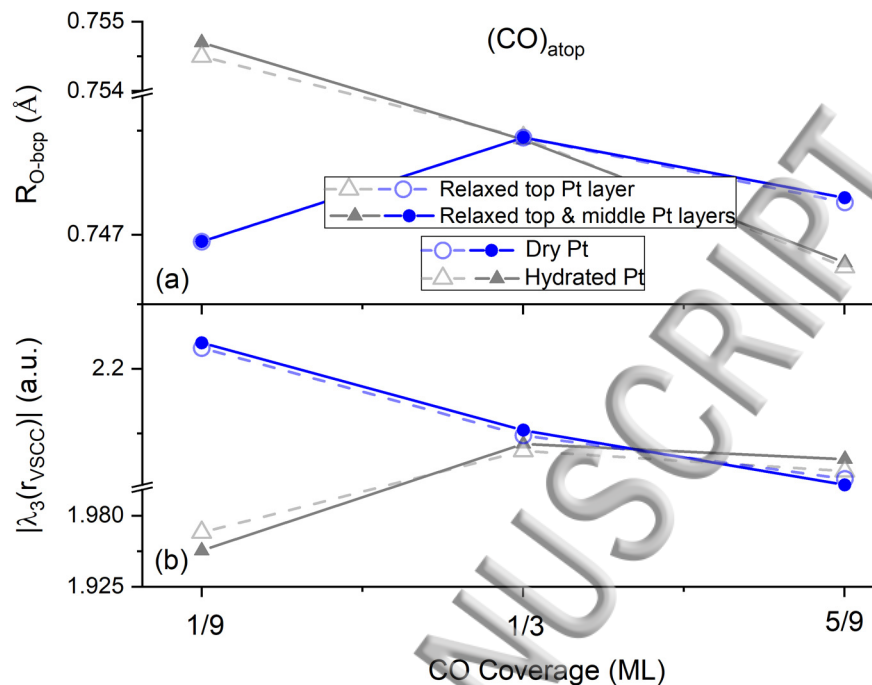
FIG. 10. QTAIM calculated properties vs. CO atop coverage on dry (blue circles) and hydrated (gray triangles, 12 water) Pt. Relaxed top substrate (hollow shapes); Both top and middle substrate layers relaxed (solid shapes): (a) $R_{O\text{-}bcp}$ and b) carbon non-bonding valence shell charge concentration (VSCC, (3, -3)) $|\lambda_3|$ value.

lengths, E_{ads}, and the $|H/\rho(\vec{r})|$ at bond critical points of atop, bridge, and 3-fold CO_{ads} on dry (blue) and hydrated (gray) Pt (12 waters). Whether dry or hydrated, the ν_{CO} and ν_{CPt} systematically downshift as the C to Pt coordination increases from atop to bridge to 3-fold, concomitant with an increase in corresponding bond lengths (Fig. 11a,b, squares and rhombus). These trends are consistent with ν_{CO} DFT calculations by Deshlahra et al. (Ref. 90) and Shan et al. (Ref. 91) (dry calculations), and observed spectra (hydrated Pt, atop and bridge sites).[109] Thus, our ν_{CO} and ν_{CPt}

shifts confirm internal CO_{ads} and C-Pt bond weakening with increased C to Pt coordination: This is consistent with decreased QTAIM $|H/\rho(\vec{r})|$ at C-O and C-Pt bond critical points, and bond strengths negatively correlated to coordination number (Fig. 11c,d). The negative correlation is further supported by changes in the $\rho(\vec{r})$ and $\nabla^2\rho(\vec{r})$ at the above bond critical points (Fig. S3) and by the C-O and C-Pt COOP (Fig. S4).

For hydrated and dry Pt, the internal CO_{ads} and C-Pt bond-strength dependence on the C to Pt coordination number was examined by QTAIM and CO_{ads} orbital analyses. The $|\lambda_i|$ (i=1, 2, 3) eigenvalues at the C-O and C-Pt bond critical points all decrease with increased coordination, in contrast to atop adsorptions (3.1 and 3.2) at various CO coverages and hydrations. The diminishing of all $|\lambda_i|$ values at the C-Pt bond critical point, and the $|\lambda_3|$ at the VSCC carbon non-bonding location (Fig. S5), are attributed to an increase in bond critical points per Pt, as the C to Pt coordination increases.

Both $\tilde{\sigma}$- and $\tilde{\pi}$-systems weaken the internal CO_{ads} and C-Pt bonds as the C to Pt coordination increases. For CO_{ads} atop vs. bridge and three-fold sites, the $4\tilde{\sigma}$ and $5\tilde{\sigma}$ orbital polarizations increase towards carbon and oxygen, respectively. This strengthens both the internal CO_{ads} bond and the C-Pt bond ($4\tilde{\sigma}$ and $5\tilde{\sigma}$ orbitals are bonding to the metal). However, the increased CO contributions to the entire $\tilde{\sigma}$-system (mostly due increased CO contributions to the $d_{\tilde{\sigma}}$-band, Table I) more than offsets bond strengthening due to changes in the $4\tilde{\sigma}$ and $5\tilde{\sigma}$ polarizations. The decrease of the λ_3 eigenvalue, at the C-O bond critical point, as the C to Pt coordination increases, is consistent with C-O σ bond weakening.

The overall C-O $\tilde{\pi}$-system weakens the bond with increased coordination: The CO contributions to the $2\tilde{\pi}^*$-and $d_{\tilde{\pi}}$-bands increase *and* the CO contribution to the $1\tilde{\pi}$ orbital

31

decreases. In summary, both phenomenological models show that increased C to Pt coordination

weakens the internal CO_{ads} bond (Table I). The C-Pt bond also weakens as CO contributions to the
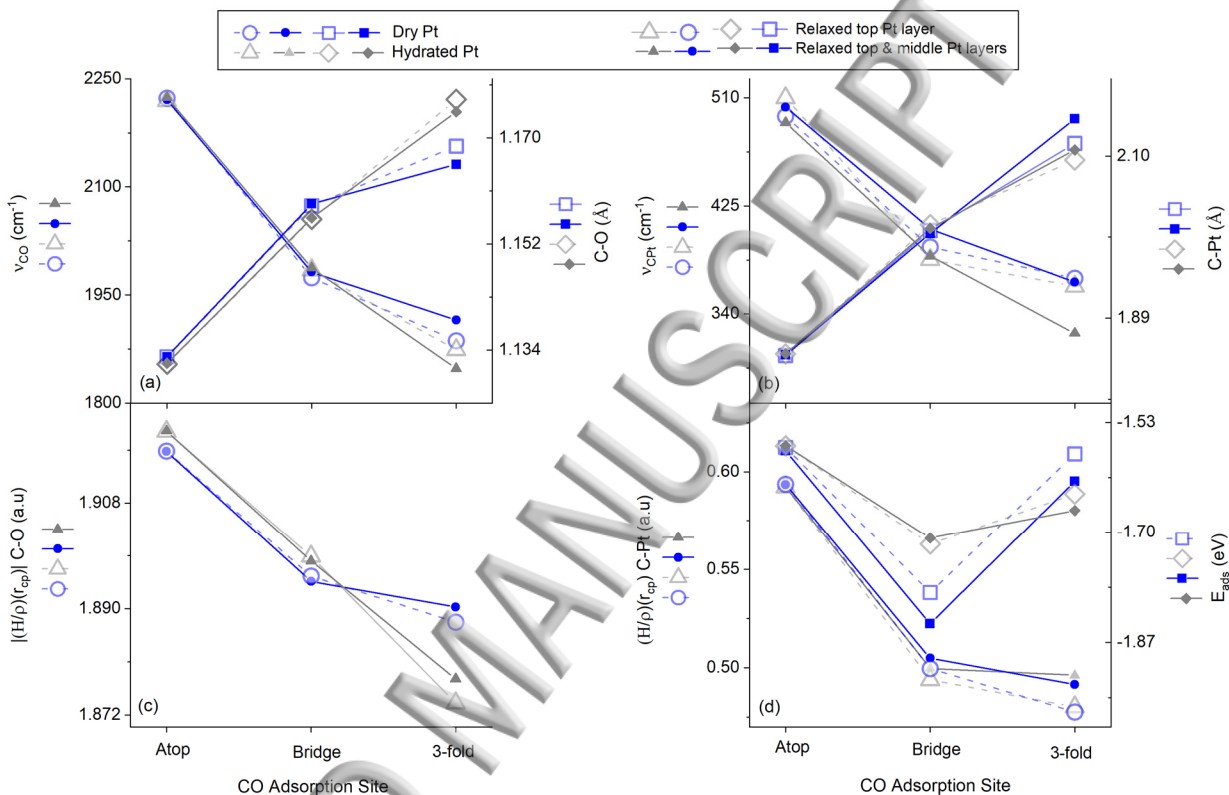
FIG. 11. DFT and QTAIM properties for CO_{ads} atop, bridge, and three-fold at 5/9 ML CO. Dry
(blue), hydrated (gray, 12 water), relaxed Pt top layer (hollow shapes) and relaxed top and middle
Pt layers (solid shapes): (a) ν_{CO} (circles and triangles) and C-O (squares and rhombus) (b) ν_{CPt}
(circles and triangles) and C-Pt (squares and rhombus), (c) $(H/\rho)(\vec{r})$ at the C-O critical points
(circles and triangles), and (d) $(H/\rho)(\vec{r})$ at the C-Pt critical points (circles and triangles) and E_{ads}
(squares and rhombus).

Pt antibonding bands (i.e., $d_{\tilde{\sigma}}$ and $d_{\tilde{\pi}}$) increases. All the above are consistent with decreased $|\lambda_1|$ and $|\lambda_2|$ eigenvalues at both the C-O and C-Pt bond critical points.

4. CONCLUSIONS

CO_ads at low coverage: At low CO_ads coverage, water co-adsorption weakens the sums of the C-O $\tilde{\sigma}$- and $\tilde{\pi}$-system orbitals. The resulting internal CO_ads bond weakening is concomitant with C-Pt bond strengthening. These co-adsorption net-effects increase with hydration and are consistent with observed shifts on ν_{CO} and ν_{CPt}, and $\rho(\vec{r})$, $\nabla^2\rho(\vec{r})$ and $H/\rho(\vec{r})$ evaluated at the bond critical points. We correlated the $\rho(\vec{r})$ Hessian non-zero eigenvalues $\lambda_{i,}$ (i=1, 2, 3) with changes in the $\tilde{\pi}$- and $\tilde{\sigma}$-system. Specifically, decreases in the $|\lambda_1|$ and $|\lambda_2|$ correspond to weaker C-O π bonding and decreases in the λ_3 (all at the C-O bond critical point) to weaker C-O σ bonding. The QTAIM view of internal CO_ads bond weakening, resulting from Pt surface hydration, is consistent with the 5σ donation-2π^* backdonation and the extended π-σ model.

CO_ads atop at higher coverage: Increasing CO coverage eventually precludes water co-adsorption, while strengthening the internal bond of atop CO_ads at the expense of the C-Pt bond strength. This is consistent with the classic inverse relationship of atop C-O to C-Pt stretching frequencies and with QTAIM. However, for CO_ads on dry Pt, the atop C-O bond lengths and their ν_{CO} values are not negatively correlated. Therefore, increased ν_{CO} values do not always correlate to stronger bonds as might be intuitively expected (Ref. 110).

In general, the $\rho(\vec{r})$, $\nabla^2\rho(\vec{r})$, and $H/\rho(\vec{r})$ at bond critical points *are* negatively correlated to bond lengths. In this work, when DFT calculated bond lengths and stretching frequencies are not negatively correlated, the phenomenological models cannot be reconciled with QTAIM results. However, because of the direct relationship between the $\tilde{\pi}$- and the $\tilde{\sigma}$-orbitals and the λ_i at the C-

33

bond critical points, the λ_i values can be used as inputs to phenomenological models to obtain an accurate description of how bond strengths vary with coverages. This demonstrates, as a highlight of this work, a powerful synergy between QTAIM and phenomenological models.

CO_{ads} bridge and 3-fold vs. atop. Both QTAIM and CO_{ads} orbital analyses confirm weakening of both the internal C_{ads} and C-Pt bonds with increased Pt coordination, in agreement with spectroscopic observations, and the weakening of both the $\tilde{\pi}$- and the $\tilde{\sigma}$-systems. The above are all consistent with decreased λ_i at C-O and C-Pt bond critical points. The CO_{ads} orbital analyses show weakening of the C-Pt bond due to increased CO contributions to the C-Pt antibonding $d_{\tilde{\sigma}}$ and $d_{\tilde{\pi}}$-bands. These effects more than offset the C-Pt bonding, caused by the remaining orbitals/bands of the $\tilde{\pi}$- and the $\tilde{\sigma}$-systems.

These conclusions can be extended to other similar systems. *Augmentation of the extended π-σ model with QTAIM provides a computational method and basis set independent technique for analyzing adsorption.*

SUPPLEMENTARY MATERIAL. See supplementary material for calculated ν_{CO}, alternative expressions for CO contributions to the $\tilde{\sigma}$-system relative to number of integrating waters, and additional QTAIM properties at atop, bridge, and three-fold sites.

ACKNOWLEDGMENTS

5. REFERENCES

[1] J. W. T. Grubb, (Google Patents, 1959).
[2] S. Gilman, J. Phys. Chem. A **68**, 70 (1964).
[3] T. Frelink, W. Visscher, and J. A. R. van Veen, Surf. Sci. **335**, 353 (1995).
[4] N. Loupe, J. Doan, and E. S. Smotkin, Catal. Today **283**, 11 (2017).

[5] E. Evarts, I. Kendrick, B. L. Wallstrom, T. Mion, M. Abedi, N. Dimakis, and E. S. Smotkin, ACS Catal. **2**, 701 (2012).

[6] B. Hammer, Y. Morikawa, and J. K. Nørskov, Phys. Rev. Lett. **76**, 2141 (1996).

[7] N. Dimakis, H. Iddir, R. R. Diaz-Morales, R. Liu, G. Bunker, E.-H. Chung, and E. S. Smotkin, J. Phys. Chem. B **109**, 1839 (2005).

[8] G. Blyholder, J. Phys. Chem. **68**, 2772 (1964).

[9] P. Bennich, T. Wiell, O. Karis, M. Weinelt, N. Wassdahl, A. Nilsson, M. Nyberg, L. G. M. Pettersson, J. Stöhr, and M. Samant, Phys. Rev. B **57**, 9274 (1998).

[10] A. Föhlisch, M. Nyberg, J. Hasselström, O. Karis, L. G. M. Pettersson, and A. Nilsson, Phys. Rev. Lett. **85**, 3309 (2000).

[11] A. Föhlisch, M. Nyberg, P. Bennich, L. Triguero, J. Hasselström, O. Karis, L. G. M. Pettersson, and A. Nilsson, J. Chem. Phys. **112**, 1946 (2000).

[12] A. Föhlisch, J. Hasselström, P. Bennich, N. Wassdahl, O. Karis, A. Nilsson, L. Triguero, M. Nyberg, and L. Pettersson, Phys. Rev. B **61**, 16229 (2000).

[13] A. Nilsson, M. Weinelt, T. Wiell, P. Bennich, O. Karis, N. Wassdahl, J. Stohr, and M. G. Samant, Phys. Rev. Lett. **78**, 2847 (1997).

[14] N. Dimakis, M. Cowan, G. Hanson, and E. S. Smotkin, J. Phys. Chem. C **113**, 18730 (2009).

[15] N. Dimakis, T. Mion, and E. S. Smotkin, J. Phys. Chem. C **116**, 21447 (2012).

[16] N. Dimakis, N. E. Navarro, T. Mion, and E. S. Smotkin, J. Phys. Chem. C **118**, 11711 (2014).

[17] N. Dimakis, F. A. Flor, N. E. Navarro, A. Salgado, and E. S. Smotkin, J. Phys. Chem. C **120**, 10427 (2016).

[18] J. W. Russell, J. Overend, K. Scanlon, M. Severson, and A. Bewick, J. Phys. Chem. **86**, 3066 (1982).

[19] C. S. Kim, W. J. Tornquist, and C. Korzeniewski, J. Chem. Phys. **101**, 9113 (1994).

[20] C. S. Kim, and C. Korzeniewski, Anal. Chem. **69**, 2349 (1997).

[21] G. Blyholder, J. Vac. Sci. Technol. **11**, (1974).

[22] F. Illas, S. Zurita, A. Marquez, and J. Rubio, Surf. Sci. **376**, 279 (1997).

[23] N. Dimakis, T. Mion, and E. S. Smotkin, J. Phys. Chem. C **116**, 21447 (2012).

[24] G. Rangelov, N. Memmel, E. Bertel, and V. Dose, Surf. Sci. **251**, 965 (1991).

[25] P. Ferrari, L. M. Molina, V. E. Kaydashev, J. A. Alonso, P. Lievens, and E. Janssens, Angew. Chem. **128**, 11225 (2016).

[26] L. Foppa, C. Copéret, and A. Comas-Vives, J. Am. Chem. Soc. **138**, 16655 (2016).

[27] W. T. Cahyanto, W. Widanarto, G. Shukri, and H. Kasai, Phys. Scr. **91**, 025803 (2016).

[28] Y.-W. Huang, and S.-L. Lee, Chem. Phys. Lett. **530**, 64 (2012).

[29] M. Jabłoński, and M. Palusiak, J. Phys. Chem. A **114**, 2240 (2010).

[30] CRYSPLOT, an online tool to visualize computed properties of periodic systems, see http://crysplot.crystalsolutions.eu/index.html

[31] D. Vega, and D. Almeida, J. Comput. Methods Sci. Eng. **14**, 131 (2014).

[32] R. F. W. Bader, P. J. MacDougall, and C. D. H. Lau, J. Am. Chem. Soc. **106**, 1594 (1984).

[33] Y. Aray, and J. Rodríguez, Can. J. Chem. **74**, 1014 (1996).

[34] Y. Aray, and J. Rodriguez, Surf. Sci. **405**, L532 (1998).

[35] Y. Aray, J. Rodriguez, J. Rivero, and D. Vega, Surf. Sci. **441**, 344 (1999).

[36] B. Rees, and A. Mitschler, J. Am. Chem. Soc. **98**, 7918 (1976).

[37] P. Macchi, D. M. Proserpio, and A. Sironi, J. Am. Chem. Soc. **120**, 13429 (1998).

[38] P. Macchi, and A. Sironi, Coord. Chem. Rev. **238**, 383 (2003).

[39] K. Morokuma, J. Chem. Phys. **55**, 1236 (1971).

[40] K. Kitaura, and K. Morokuma, Int. J. Quantum Chem. **10**, 325 (1976).

[41] P. S. Bagus, K. Hermann, and C. W. Bauschlicher, J. Chem. Phys. **80**, 4378 (1984).

[42] P. S. Bagus, K. Hermann, and C. W. Bauschlicher, J. Chem. Phys. **81**, (1984).

[43] E. D. Glendening, and A. Streitwieser, J. Chem. Phys. **100**, 2900 (1994).

[44] E. D. Glendening, J. Am. Chem. Soc. **118**, 2473 (1996).

[45] E. D. Glendening, J. Phys. Chem. A **109**, 11936 (2005).

[46] R. Z. Khaliullin, E. A. Cobar, R. C. Lochan, A. T. Bell, and M. Head-Gordon, J. Phys. Chem. A **111**, 8753 (2007).

[47] P. R. Horn, E. J. Sundstrom, T. A. Baker, and M. Head-Gordon, J. Chem. Phys. **138**, 134119 (2013).

[48] M. Raupach, and R. Tonner, J. Chem. Phys. **142**, 194105 (2015).

[49] P. S. Bagus, and G. Pacchioni, Surf. Sci. **278**, 427 (1992).

[50] P. S. Bagus, C. J. Nelin, and C. W. Bauschlicher, J. Vac. Sci. Technol. A **2**, 905 (1984).

[51] D. Curulla, A. Clotet, J. M. Ricart, and F. Illas, J. Phys. Chem. B **103**, 5246 (1999).

[52] C. N. Hernández, and C. M. Zicovich-Wilson, J. Chem. Phys. **124**, 194105 (2006).

[53] G. Pacchioni, T. Minerva, and P. S. Bagus, Surf. Sci. **275**, 450 (1992).

[54] P. Hohenberg, and W. Kohn, Phys. Rev. **136**, B864 (1964).

[55] W. Kohn, and L. J. Sham, Phys. Rev. **140**, A1133 (1965).

[56] R. S. Mulliken, J. Chem. Phys. **23**, 1833 (1955).

[57] D. Ogletree, M. Van Hove, and G. Somorjai, Surf. Sci. **173**, 351 (1986).

[58] G. S. Blackman, M. L. Xu, D. F. Ogletree, M. A. Van Hove, and G. A. Somorjai, Phys. Rev. Lett. **61**, 2352 (1988).

[59] H. Hopster, and H. Ibach, Surf. Sci. **77**, 109 (1978).

[60] H. Steininger, S. Lehwald, and H. Ibach, Surf. Sci. **123**, 264 (1982).

[61] B. Hayden, K. Kretzschmar, A. Bradshaw, and R. Greenler, Surf. Sci. **149**, 394 (1985).

[62] M.-L. Bocquet, and P. Sautet, Surf. Sci. **360**, 128 (1996).

[63] Jmol, an open-sourse Java viewer for chemical structures in 3D, see http://www.jmol.org/

[64] P. J. Feibelman, B. Hammer, J. K. Nørskov, F. Wagner, M. Scheffler, R. Stumpf, R. Watwe, and J. Dumesic, J. Phys. Chem. B **105**, 4018 (2001).

[65] R. Dovesi, V. Saunders, C. Roetti, R. Orlando, C. Zicovich-Wilson, F. Pascale, B. Civalleri, K. Doll, N. Harrison, and I. Bush, *CRYSTAL14 User's Manual* University of Torino: Torino,

[66] R. Dovesi, R. Orlando, A. Erba, C. M. Zicovich-Wilson, B. Civalleri, S. Casassa, L. Maschio, M. Ferrabone, M. De La Pierre, and P. D'Arco, Int. J. Quantum Chem. **114**, 1287 (2014).

[67] M. Ernzerhof, and G. E. Scuseria, J. Chem. Phys. **110**, 5029 (1999).

[68] C. Adamo, and V. Barone, J. Chem. Phys. **110**, 6158 (1999).

[69] F. Pascale, C. M. Zicovich-Wilson, F. Lopez Gejo, B. Civalleri, R. Orlando, and R. Dovesi, J. Comput. Chem. **25**, 888 (2004).

[70] D. Andrae, U. Haeussermann, M. Dolg, H. Stoll, and H. Preuss, Theor. Chim. Acta **77**, 123 (1990).

[71] Stuttgart/Cologne energy-consistent (*ab initio*) pseudopotentials suitable for DFT calculations, see http://www.uni-stuttgart.de/theochem/

[72] K. Doll, Surf. Sci. **573**, 464 (2004).

[73] M. F. Peintinger, D. V. Oliveira, and T. Bredow, J. Comput. Chem. **34**, 451 (2013).

[74] H. J. Monkhorst, and J. D. Pack, Phys. Rev. B **13**, 5188 (1976).

[75] G. Gilat, and L. Raubenheimer, Phys. Rev. **144**, 390 (1966).

[76] G. Gilat, J. Comput. Phys. **10**, 432 (1972).

[77] R. Hoffmann, Rev. Mod. Phys. **60**, 601 (1988).

[78] R. Dovesi, V. R. Saunders, C. Roetti, C. M. Zicovich-Wilson, F. Pascale, B. Civalleri, K. Doll, N. M. Harrison, I. J. Bush, P. D'Arco, M. Llunell, M. Causà, Y. Noël, L. Maschio, R. Orlando, A. Erba, M. Rérat, and S. Casassa, *CRYSTAL17 User's Manual* Univ. Torino, Torino, 2017),

[79] C. Stampfl, and M. Scheffler, Phys. Rev. B **65**, 155417 (2002).

[80] S. F. Boys, and F. d. Bernardi, Mol. Phys. **19**, 553 (1970).

[81] F. B. Van Duijneveldt, J. G. van Duijneveldt-van de Rijdt, and J. H. van Lenthe, Chem. Rev. **94**, 1873 (1994).

[82] C. Gatti, User's manual **CNR-CSRSRC, Milano**, (1996).

[83] C. Gatti, V. Saunders, and C. Roetti, J. Chem. Phys. **101**, 10686 (1994).

[84] C. Gatti, Z. Kristallogr. Cryst. Mater. **220**, 399 (2005).

[85] M. T. Ruggiero, A. Erba, R. Orlando, and T. M. Korter, Phys. Chem. Chem. Phys. **17**, 31023 (2015).

[86] R. Dronskowski, and P. E. Bloechl, J. Phys. Chem. **97**, 8617 (1993).

[87] A. Grechnev, R. Ahuja, and O. Eriksson, J. Phys. Condens. Matter **15**, 7751 (2003).

[88] I. Dabo, A. Wieckowski, and N. Marzari, J. Am. Chem. Soc. **129**, 11045 (2007).

[89] M. T. M. Koper, T. E. Shubina, and R. A. van Santen, J. Phys. Chem. B **106**, 686 (2002).

[90] P. Deshlahra, J. Conway, E. E. Wolf, and W. F. Schneider, Langmuir **28**, 8408 (2012).

[91] B. Shan, Y. Zhao, J. Hyun, N. Kapur, J. B. Nicholas, and K. Cho, J. Phys. Chem. C **113**, 6088 (2009).

[92] R. Liu, H. Iddir, Q. B. Fan, G. Y. Hou, A. L. Bo, K. L. Ley, E. S. Smotkin, Y. E. Sung, H. Kim, S. Thomas, and A. Wieckowski, J. Phys. Chem. B **104**, 3518 (2000).

[93] S. C. Chang, and M. J. Weaver, J. Chem. Phys. **92**, 4582 (1990).

[94] K. Yoshimi, M.-B. Song, and M. Ito, Surf. Sci. **368**, 389 (1996).

[95] J. A. Steckel, A. Eichler, and J. Hafner, Phys. Rev. B **68**, 085416 (2003).

[96] R. M. Badger, J. Chem. Phys. **2**, 128 (1934).

[97] R. M. Badger, J. Chem. Phys. **3**, 710 (1935).

[98] J. Cioslowski, G. Liu, and R. A. M. Castro, Chem. Phys. Lett. **331**, 497 (2000).

[99] S.-C. Chang, and M. J. Weaver, Surf. Sci. **238**, 142 (1990).

[100] M. W. Severson, C. Stuhlmann, I. Villegas, and M. J. Weaver, J. Chem. Phys. **103**, 9832 (1995).

[101] C. Korzeniewski, V. Climent, and J. M. Feliu, in *Electroanalytical Chemistry*, edited by C. Zoski, and A. J. Bard (Taylor & Francis, 2012), pp. 75.

[102] C. Korzeniewski, in *Interfacial Electrochemistry*, edited by A. Wieckowski (Marcel Dekker, Inc., New York, 1999), pp. 345.

[103] S. C. Chang, and M. J. Weaver, J. Phys. Chem. **95**, 5391 (1991).

[104] C. Korzeniewski, and M. W. Severson, Spectrochim. Acta A **51A**, 499 (1995).

[105] H. Ueba, Surf. Sci. **188**, 421 (1987).

[106] D. Loffreda, D. Simon, and P. Sautet, Surf. Sci. **425**, 68 (1999).

[107] D. Curulla, A. Clotet, and J. M. Ricart, Surf. Sci. **460**, 101 (2000).

[108] M. Kaupp, B. Metz, and H. Stoll, Angew. Chem. Int. Ed. **39**, 4607 (2000).

[109] S. D. Ebbesen, B. L. Mojet, and L. Lefferts, Langmuir **22**, 1079 (2006).

[110] Y. J. Huang, S. C. Fung, W. E. Gates, and G. B. McVicker, J. Catal. **118**, 192 (1989).

Electron Density $\rho(\vec{r})$

2D view   3D view

O

C

CO-bond critical point

(a)

Gradient of Electron Density $\nabla\rho(\vec{r})$

O basin

O

CO-bond critical point

C

C basin

(b)

Laplacian of Electron Density $-\nabla^2\rho(\vec{r})$

2D view   3D view

O Lone pair

O

C

O

C

C Lone pair

(c)

CO Coverage

Water Coverage

O = 8.14 e
C = 5.72 e

1/9 ML, 0 water

(a)

O = 8.15 e
C = 5.81 e

5/9 ML, 0 water

(b)

O = 8.24 e
C = 5.82 e

1/9 ML, 12 water

(c)

O = 8.14 e
C = 5.82 e

5/9 ML, 12 water

(d)

Electron Density $\rho(\vec{r})$

O

R_{O-bcp}

C

Pt

(a)

Laplacian $-\nabla^2\rho(\vec{r})$

O

C

C-VSCC

Pt

(c)

(CO)$_{atop}$

(a)

Relaxed top Pt layer
Relaxed top & middle Pt layers

Dry Pt
Hydrated Pt

(b)

CO Coverage (ML)